Supporting Information

for

Visible to Near-Infrared Light Responsive Halochromic Hydrazones

Shefali Patra and Ivan Aprahamian*

Department of Chemistry, 6128 Burke Laboratory, Dartmouth College, Hanover, New Hampshire 03755, USA

Email: ivan.aprahamian@dartmouth.edu

Table of Contents

1 Synthesis

Supplementary Scheme S1. The synthetic route for hydrazone **1**.

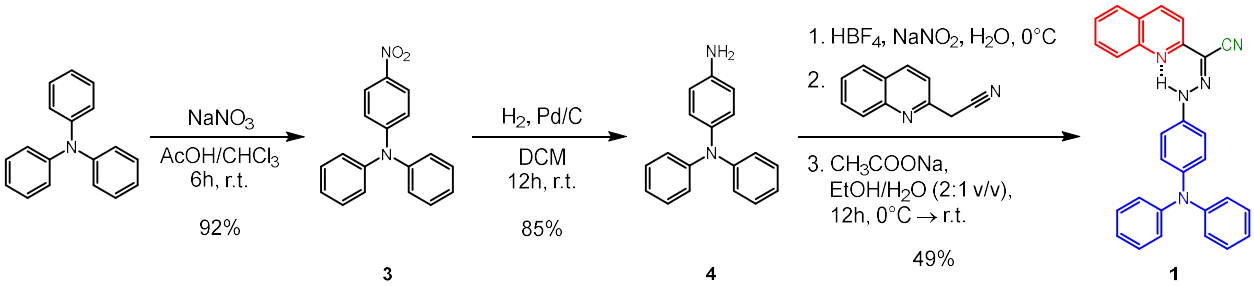

3: This compound was synthesized using a modified procedure, and its identity was confirmed by comparing the obtained ^{1}H NMR spectrum with the reported one.[S1] Sodium nitrate (175 mg, 2.06 mmol, 1.0 equiv.) was added to a mixture of triphenylamine (505 mg, 2.06 mmol, 1.0 equiv.) in glacial acetic acid (18 mL) and chloroform (6 mL). The resulting mixture was refluxed for 6h and then cooled to room temperature. The mixture was then diluted with water (50 mL) and extracted with DCM (50 mL). The organic layer was washed with saturated sodium bicarbonate solution (3 × 25 mL) and brine (25 mL), dried over Na_2SO_4, and then concentrated *in vacuo* to yield **3** as an orange solid (550 mg, 92% yield). The product was used for the next step without further purification. ^{1}H NMR (600 MHz, $CDCl_3$) δ 8.04 (d, J = 9.3 Hz, 2H), 7.37 (t, J = 7.7 Hz, 4H), 7.23 – 7.15 (m, 6H), 6.92 (d, J = 9.3 Hz, 2H).

4: This compound was synthesized using a modified procedure, and its identity was confirmed by comparing the obtained ^{1}H NMR spectrum with the reported one.[S2] Palladium on carbon (10%, 50 mg, 10 wt.%) was added to a solution of **3** (500 mg, 1.72 mmol, 1.0 equiv.) in DCM, and the mixture was stirred for 12h under hydrogen atmosphere at room temperature. The reaction mixture was then filtered through celite, and the filtrate was washed with water (3 × 25 mL) and brine (25 mL), followed by drying over Na_2SO_4. The solvent was then removed under vacuum, and the residue was subjected to silica gel column chromatography (ethyl acetate/hexane 1:9, v/v) to yield **4** as a pale violet solid (380 g, 85% yield). ^{1}H NMR (600 MHz, $CDCl_3$) δ 7.2 (t, J = 7.7 Hz, 4H), 7.03 (d, J = 7.8 Hz, 4H), 6.97 (d, J = 8.0 Hz, 2H), 6.92 (t, J = 7.1 Hz, 2H), 6.68 (d, J = 7.5 Hz, 2H), 4.13 (br, s, 2H).

1: 1.5 mL of HBF_4 (48% w/w) was added dropwise to a mixture of **4** (286 mg, 1.1 mmol, 1.5 equiv.) in 0.5 mL water. After stirring in an ice bath for 15 min, a precooled aqueous solution of sodium nitrite (76 mg, 1.1 mmol, 1.5 equiv.), was added dropwise over a period of 30 min. The diazonium salt was collected by filtration after 45 min and added to a suspension of 2-quinolylacetonitrile (123 mg, 0.73 mmol, 1.0 equiv.) and sodium acetate (361 mg, 4.4 mmol, 6.0 equiv.) in a cooled and well-stirred ethanol/water mixture (2:1 v/v, 10 mL). The reaction mixture was allowed to warm up to room temperature and stirred for 12 h, followed by the addition of 15 mL water. The mixture was extracted with DCM, and the organic phase was washed with water (3 × 25 mL) and brine (25

mL), dried over Na_2SO_4, and concentrated *in vacuo*. The residue was subjected to silica gel column chromatography (ethyl acetate/hexane, 1:9 v/v) to afford **1** as an orange solid (157 mg, 49% yield). m.p. 202.5–202.9 °C; ^{1}H NMR (600 MHz, CD_2Cl_2) δ 16.21 (s, 1H), 8.34 (d, J = 8.8 Hz, 1H), 8.05 (d, J = 8.4 Hz, 1H), 7.89 (d, J = 8.1 Hz, 1H), 7.85 – 7.79 (m, 2H), 7.63 (t, J = 7.0 Hz, 1H), 7.39 (d, J = 8.9 Hz, 2H), 7.27 (t, J = 7.4 Hz, 4H), 7.15 (d, J = 8.8 Hz, 2H), 7.09 (d, J = 8.6 Hz, 4H), 7.03 (t, J = 7.4 Hz, 2H). ^{13}C NMR (151 MHz, CD_2Cl_2) δ 152.6, 148.1, 146.0, 145.0, 138.1, 138.0, 131.2, 130.0, 128.3, 128.2, 128.0, 127.2, 125.8, 124.3, 124.2, 123.2, 120.0, 118.3, 116.6. ESI-HRMS: *m/z* found [M-H$^+$] for $C_{29}H_{22}N_5^+$ 440.1862 (calcd. 440.1875).

Supplementary Scheme S2. The synthetic route for hydrazone **2**.

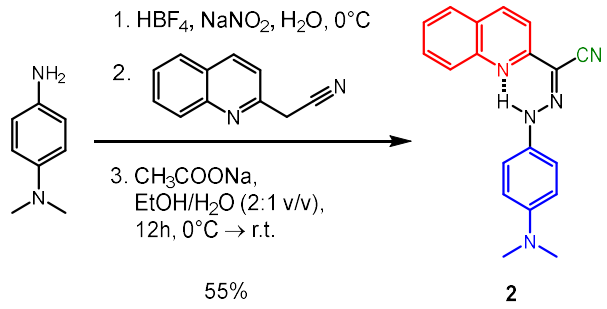

2: The compound was synthesized using a previously reported procedure, and its identity was confirmed by comparing the obtained ^{1}H NMR spectrum with the reported one.[S3] Hydrazone **2** was obtained as a reddish orange solid (127 mg, 55% yield). ^{1}H NMR (500 MHz, CD_2Cl_2) δ 16.25 (s, 1H), 8.29 (d, J = 8.8 Hz, 1H), 8.05 (d, J = 8.4 Hz, 1H), 7.87 (d, J = 8.1 Hz, 1H), 7.82 – 7.75 (m, 2H), 7.60 (t, J = 7.2 Hz, 1H), 7.39 (d, J = 9.0 Hz, 2H), 6.80 (d, J = 9.0 Hz, 2H), 2.98 (s, 6H).

2 Acid/Base Response of the Hydrazones

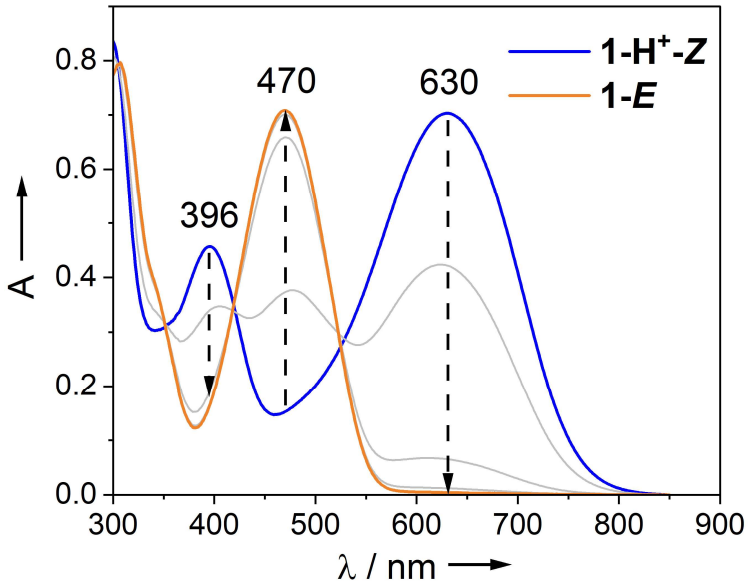

Supplementary Figure S1. UV-Vis absorption spectra for the titration of **1-H$^+$-*Z*** (2.3×10^{-5} M) with Et_3N in toluene. Changes in the major bands are highlighted. The light gray lines show the spectral changes upon the addition of Et_3N in 200 equiv. increments.

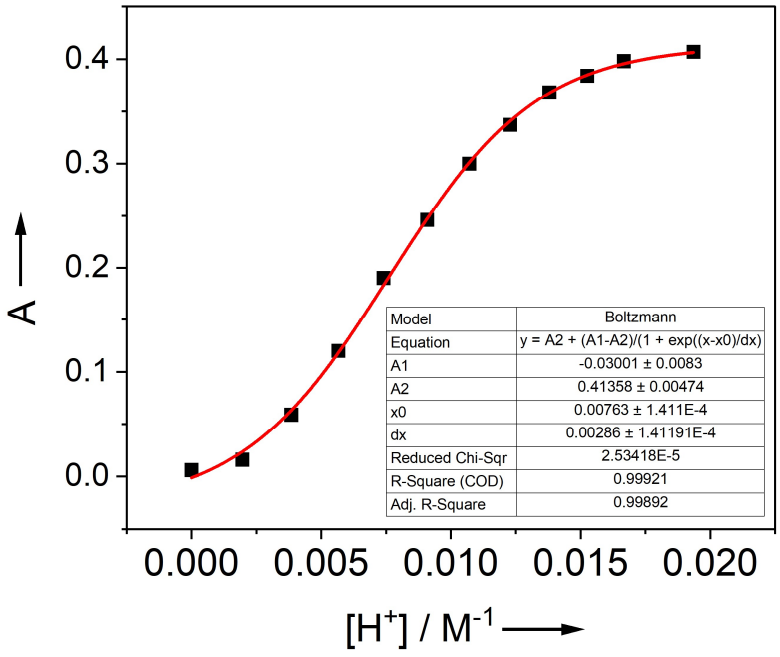

Supplementary Figure S2. Fitting curve for the titration of **1-*E*** (2.0×10^{-5} M) with TFA in toluene. The plot is of the absorbance (at λ_{max} = 630 nm) of **1-H$^+$-*Z*** as a function of H^+ concentration. The pK_{aH} value of **1** was determined to be 2.05 ± 0.06 based on three consecutive measurements.

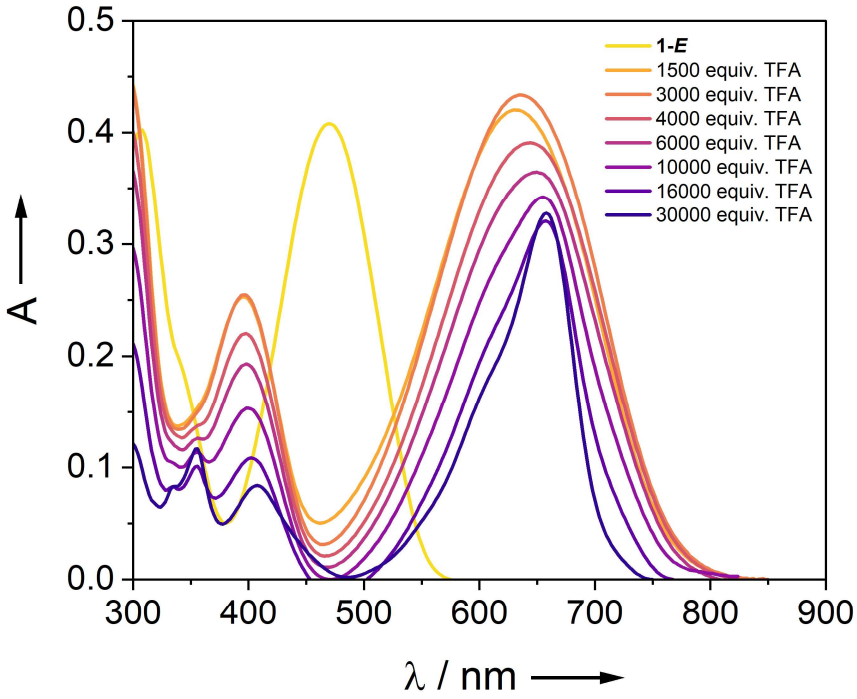

Supplementary Figure S3. UV-Vis absorption spectra for the titration of **1-*E*** (1.6×10^{-5} M) with excess TFA in toluene.

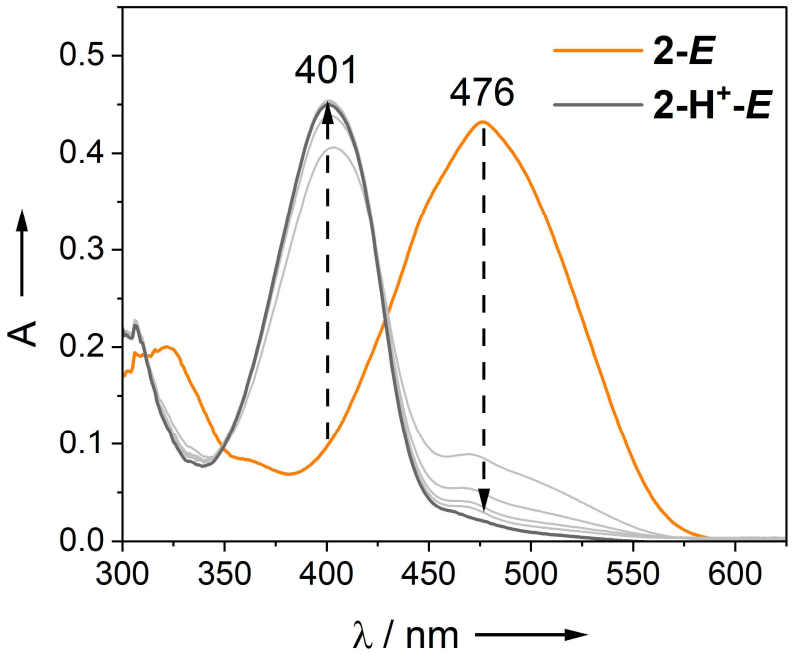

Supplementary Figure S4. UV-Vis absorption spectra for the titration of **2-*E*** (2.0×10^{-5} M) with TFA to produce **2-H$^+$-*E*** in toluene. Changes in the major bands are highlighted. The light gray lines show the spectral changes upon the addition of TFA in 40 equiv. increments.

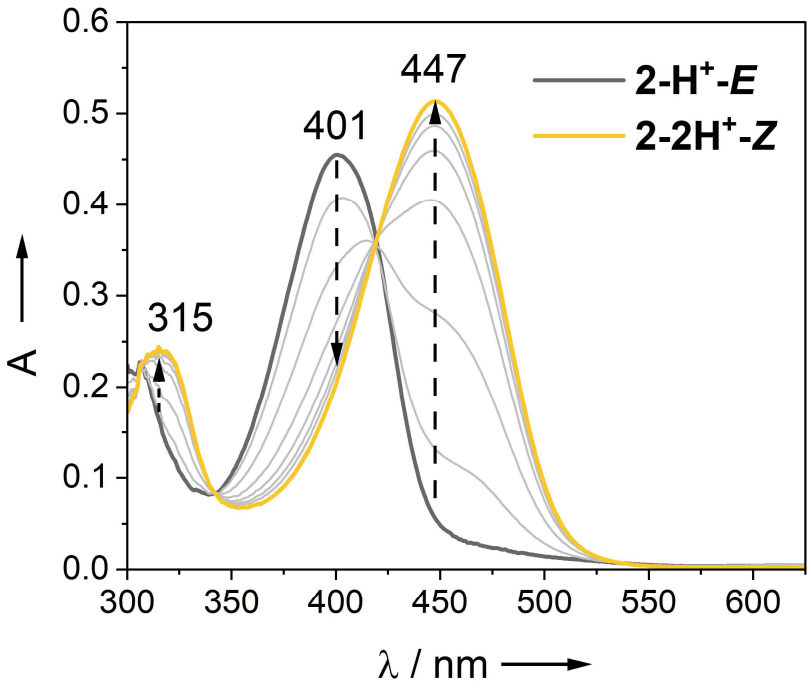

Supplementary Figure S5. UV-Vis absorption spectra for the titration of **2-H$^+$-*E*** (1.99×10^{-5} M) with TFA to produce **2-2H$^+$-*Z*** in toluene. Changes in the major bands are highlighted. The light gray lines show spectral changes upon the addition of TFA in 500 equiv. increments.

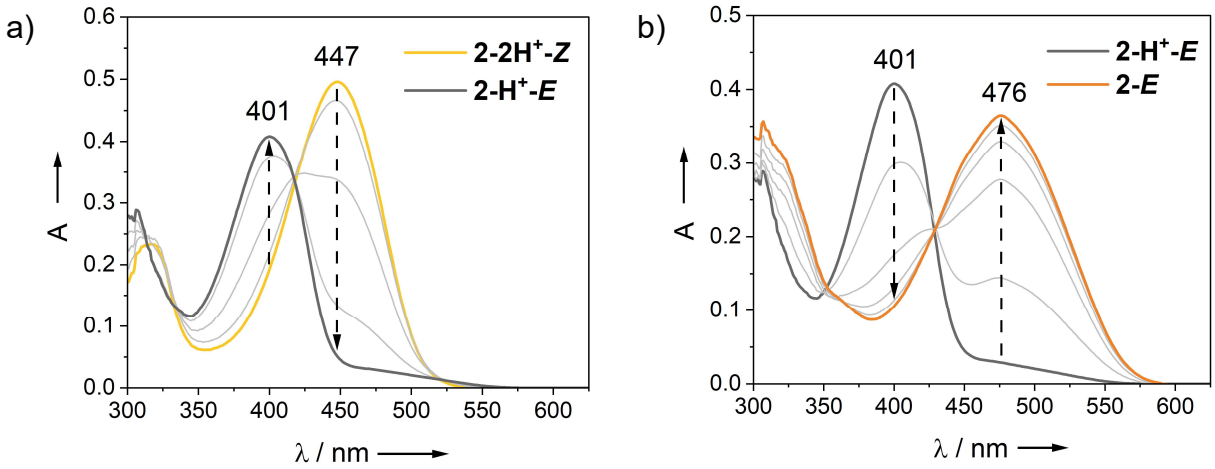

Supplementary Figure S6. UV-Vis absorption spectra for the titration of **2-2H$^+$-*Z*** (1.95×10^{-5} M) with Et_3N in toluene: (a) conversion of **2-2H$^+$-*Z*** to **2-H$^+$-*E***, and (b) the subsequent conversion of **2-H$^+$-*E*** to **2-*E***. Changes in the major bands are highlighted. The light gray lines show spectral changes upon the addition of Et_3N in 500 equiv. increments.

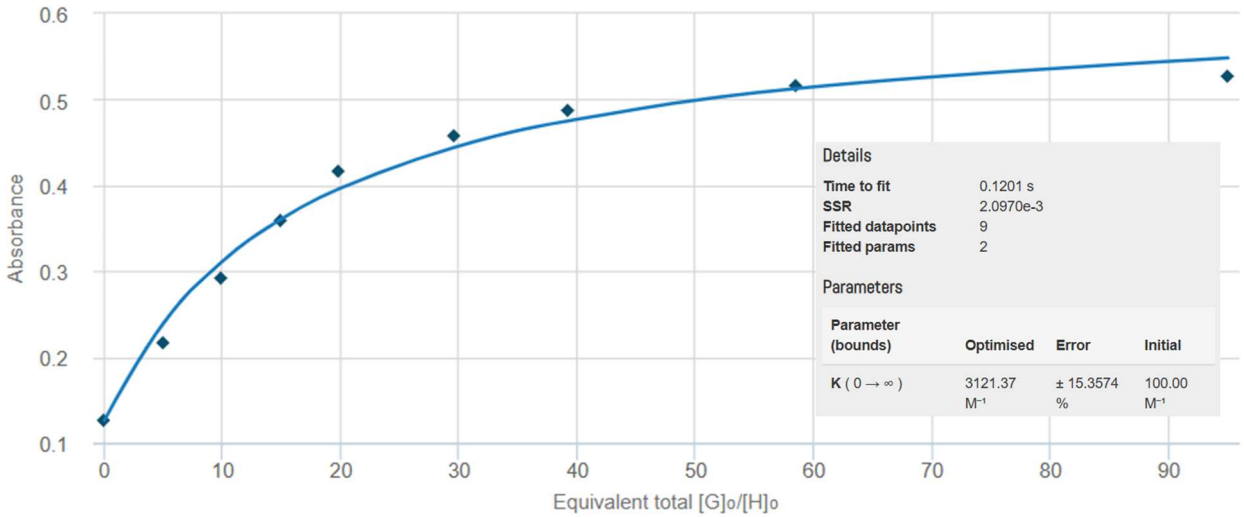

Supplementary Figure S7. Fitting curve for the titration of **2-*E*** (2.0×10^{-5} M) with TFA in toluene based on a 1:1 binding model using BindFit v0.5. Absorbance of **2-H$^+$-*E*** was monitored at λ_{max} = 401 nm. The pK_{aH1} value of **2** was determined to be 3.48 ± 0.02 based on three consecutive measurements.[S4]

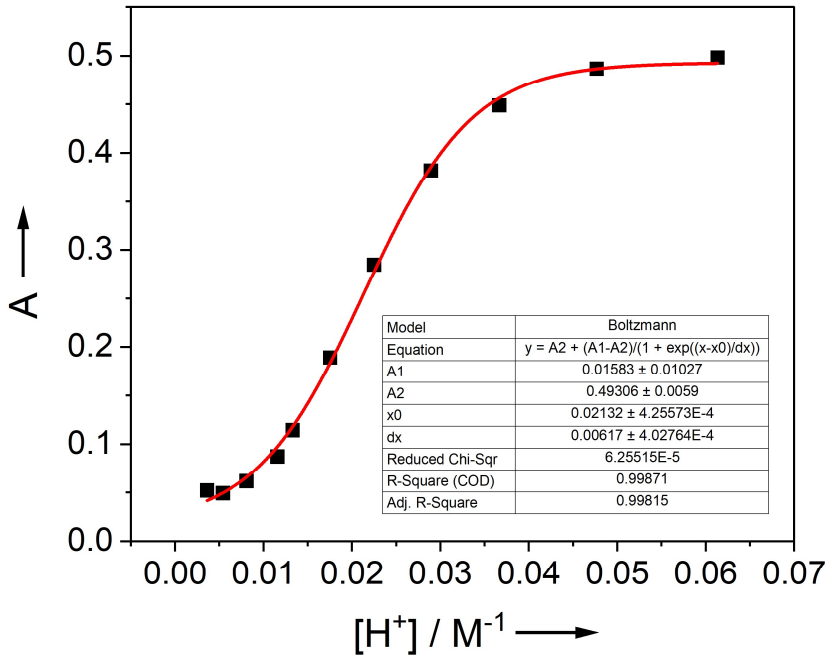

Supplementary Figure S8. Fitting curve for the titration of **2-H$^+$-*E*** (1.99×10^{-5} M) with TFA in toluene. The plot is of the absorbance (at λ_{max} = 447 nm) of **2-2H$^+$-*Z*** as a function of H^+ concentration. The pK_{aH2} value of **2** was determined to be 1.72 ± 0.04 based on three consecutive measurements.

3 Photoisomerization Studies

The photoisomerization process was studied using UV-Vis spectroscopy. Spectrophotometric grade solvents were used for the studies. A solution (2 mL) of the compound in toluene was prepared and transferred into a 1.0 cm quartz cuvette. The solution was then irradiated, and UV-Vis spectra were recorded after reaching the appropriate photostationary state (PSS).

Isomerization cycles were obtained by alternating the irradiation wavelength between the appropriate wavelengths or by alternating between irradiation and thermal isomerization in the dark and monitoring the change in UV-Vis absorbance. The spectra of the pure (>99%) *Z* isomers of **1**, **2**, and **2-H**$^+$ and the pure (>99%) *E* isomer of **2-2H**$^+$ were extrapolated by following previously reported methods. [S5,S6]

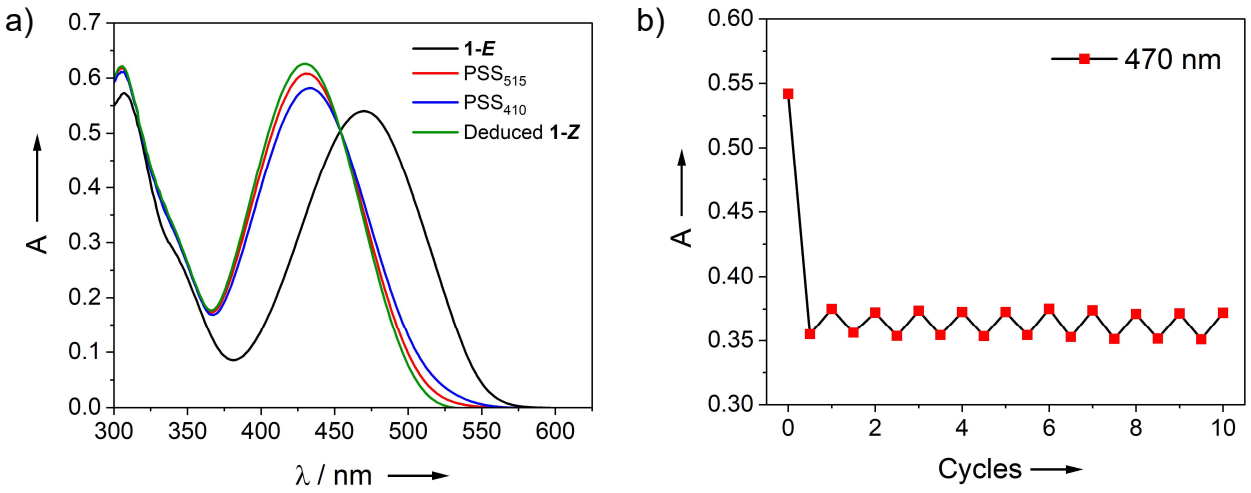

Supplementary Figure S9. (a) Light-induced *Z*/*E* isomerization of **1** (2.0×10^{-5} M) in toluene. (b) Photoisomerization cycles of **1** (2.0×10^{-5} M) in toluene at 294 K. The absorbance change at 470 nm was monitored while alternating the irradiation wavelength between 515 and 410 nm.

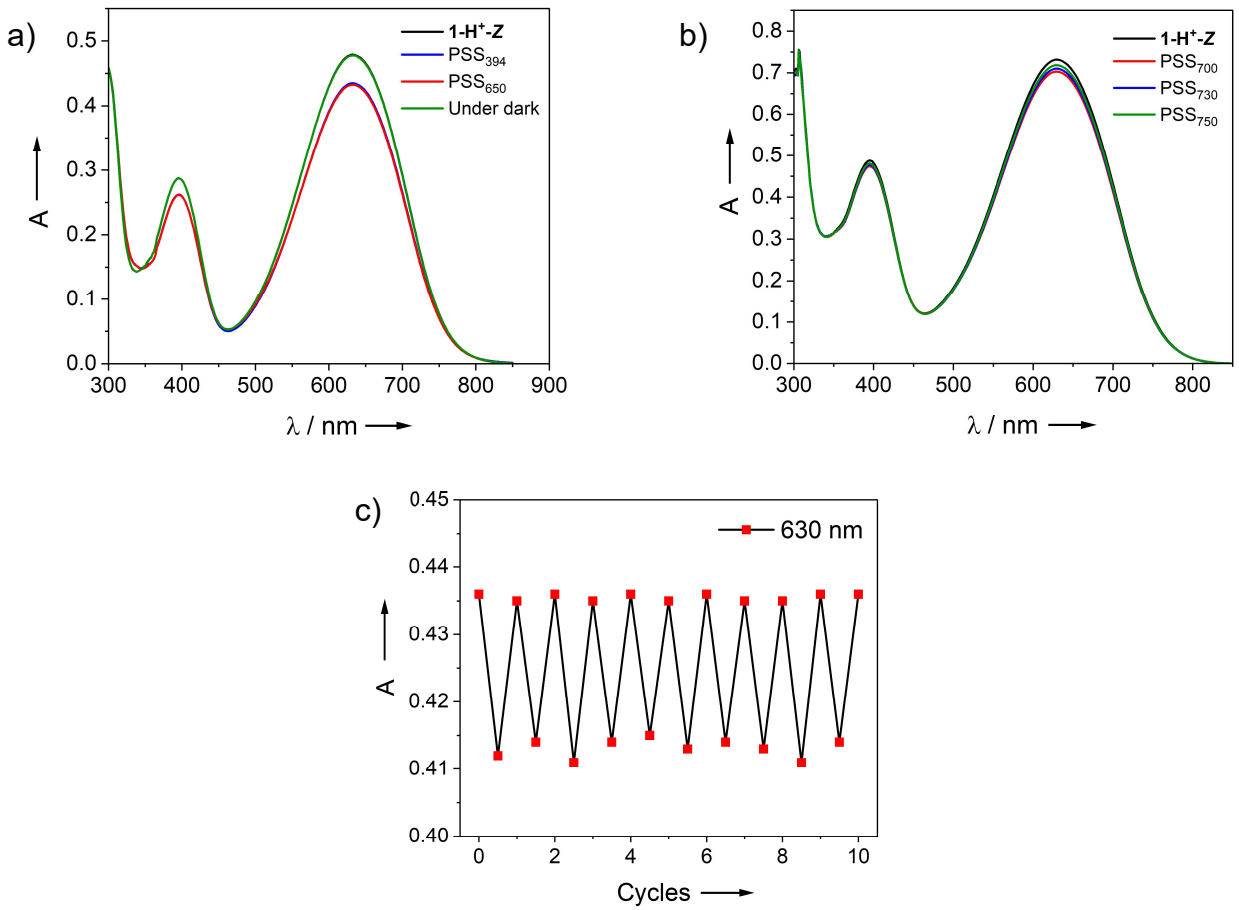

Supplementary Figure S10. (a) Light-induced *Z*/*E* isomerization of **1-H**$^+$ (1.57×10^{-5} M) in toluene. (b) Response of **1-H**$^+$ (2.40×10^{-5} M) to NIR light irradiation in toluene. (c) Photoisomerization cycles of **1-H**$^+$ (1.43×10^{-5} M) in toluene at 294 K. The absorbance change at 630 nm was monitored while alternating between 650 nm irradiation and storage in the dark.

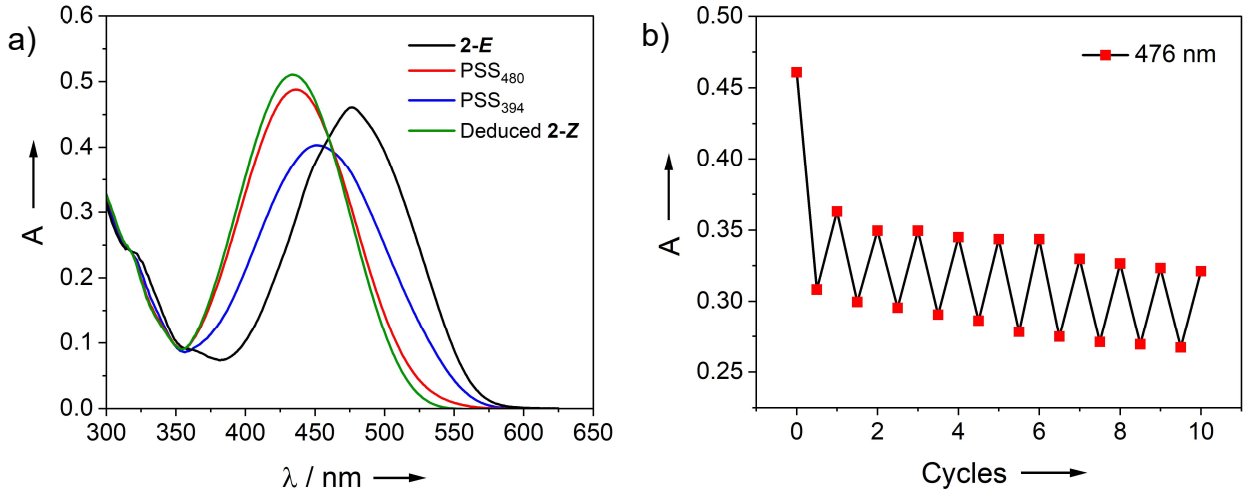

Supplementary Figure S11. (a) Light-induced *Z*/*E* isomerization of **2** (2.0×10^{-5} M) in toluene. (b) Photoisomerization cycles of **2** (2.0×10^{-5} M) in toluene at 294 K. The absorbance change at 476 nm was monitored while alternating the irradiation wavelength between 480 and 394 nm.

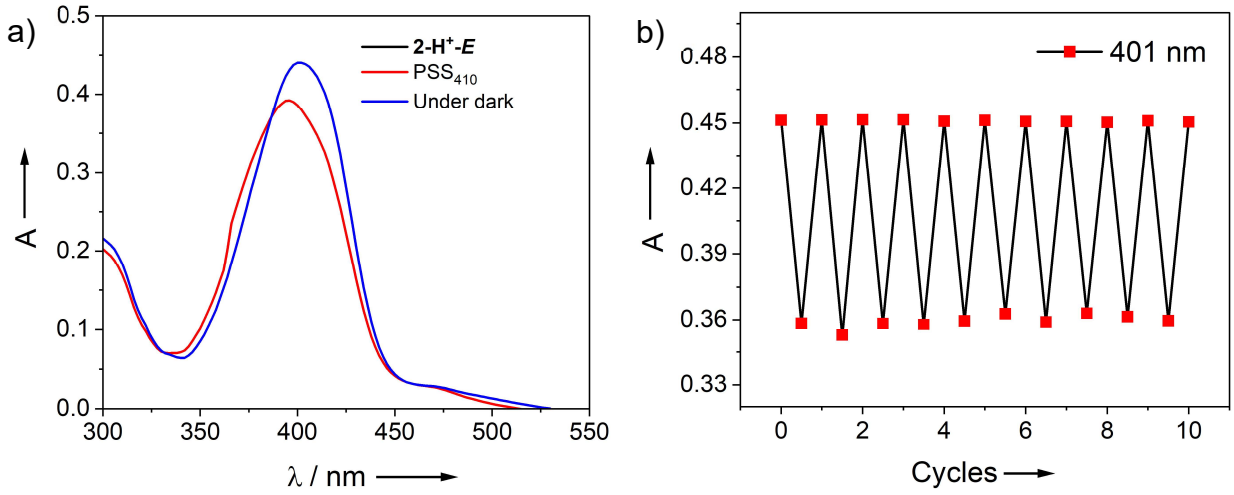

Supplementary Figure S12. (a) Light-induced *Z*/*E* isomerization of **2-H**$^+$ (1.99×10^{-5} M) in toluene. (b) Photoisomerization cycles of **2-H**$^+$ (1.99×10^{-5} M) in toluene at 294 K. The absorbance change at 401 nm was monitored while alternating between 410 nm irradiation and storage in the dark.

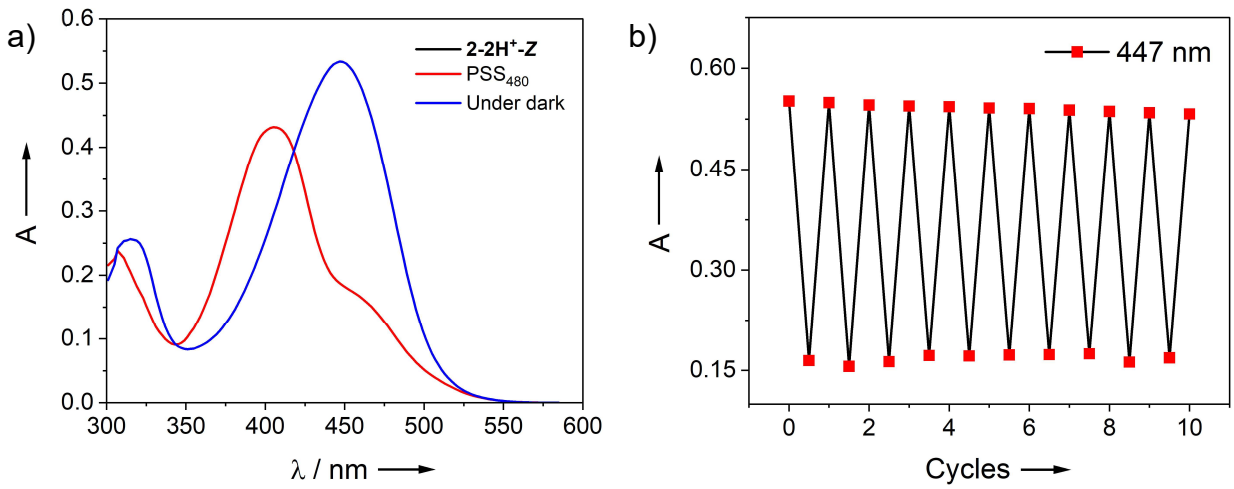

Supplementary Figure S13. (a) Light-induced *Z*/*E* isomerization of **2-2H**$^+$ (1.95×10^{-5} M) in toluene. (b) Photoisomerization cycles of **2-2H**$^+$ (1.95×10^{-5} M) in toluene at 294 K. The absorbance change at 447 nm was monitored while alternating between 480 nm irradiation and storage in the dark.

4 Photostationary States (PSS) Studies

The PSSs were quantified using UV-Vis spectroscopy following a previously reported method.[S5] Briefly, the negative photochromism of hydrazones enables the estimation of the spectrum of the metastable isomer (*E* for **2-2H**$^+$ and *Z* for **1**, **2**, and **2-H**$^+$) from the spectra of the stable isomer (*Z* for **2-2H**$^+$ and *E* for **1**, **2**, and **2-H**$^+$), and a recorded PSS spectrum. Starting from the measured spectra for the stable isomer and a PSS spectrum, the ratio of the absorbance values at PSS and for the stable isomer spectrum (*e.g.*, Abs(PSS)/Abs(*Z*) for **2-2H**$^+$) is plotted against the wavelength. As depicted in Supplementary Figures S14–S17, the area where the obtained curve remains horizontal represents the region where only the metastable isomer absorbs and the stable isomer does not. The value of Abs(PSS)/Abs(*E*) (for **1**, **2**, and **2-H**$^+$) or Abs(PSS)/Abs(*Z*) (for **2-2H**$^+$) at this wavelength corresponds to the relative content of the *E* or the *Z* isomer, respectively at the relevant PSS.

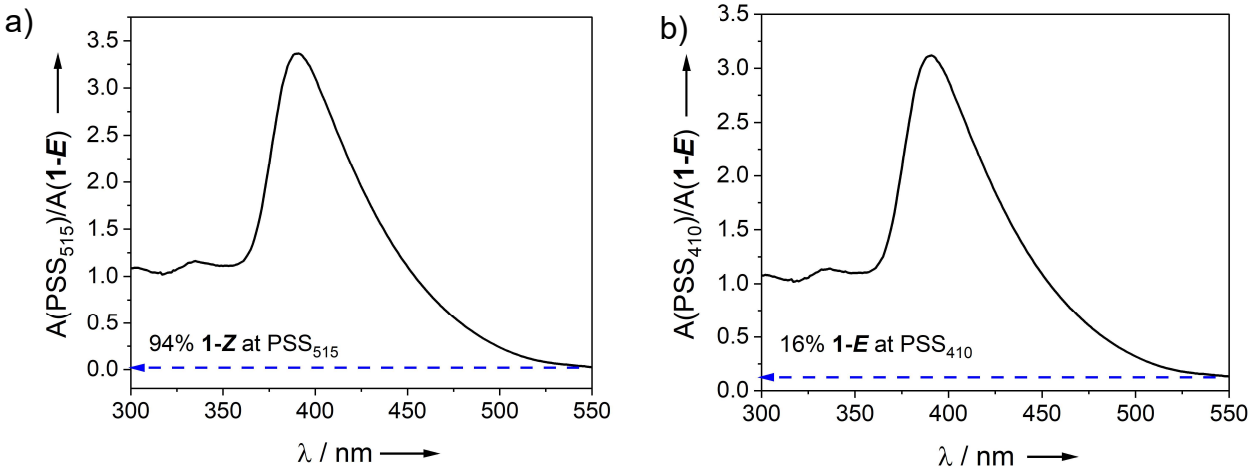

Supplementary Figure S14. Determination of the composition of (a) PSS_{515} and (b) PSS_{410} of hydrazone **1**.

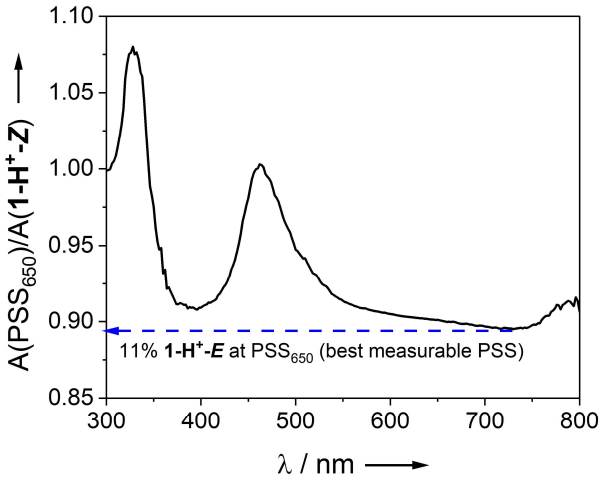

Supplementary Figure S15. Determination of the composition of PSS_{650} of hydrazone **1-H**$^+$.

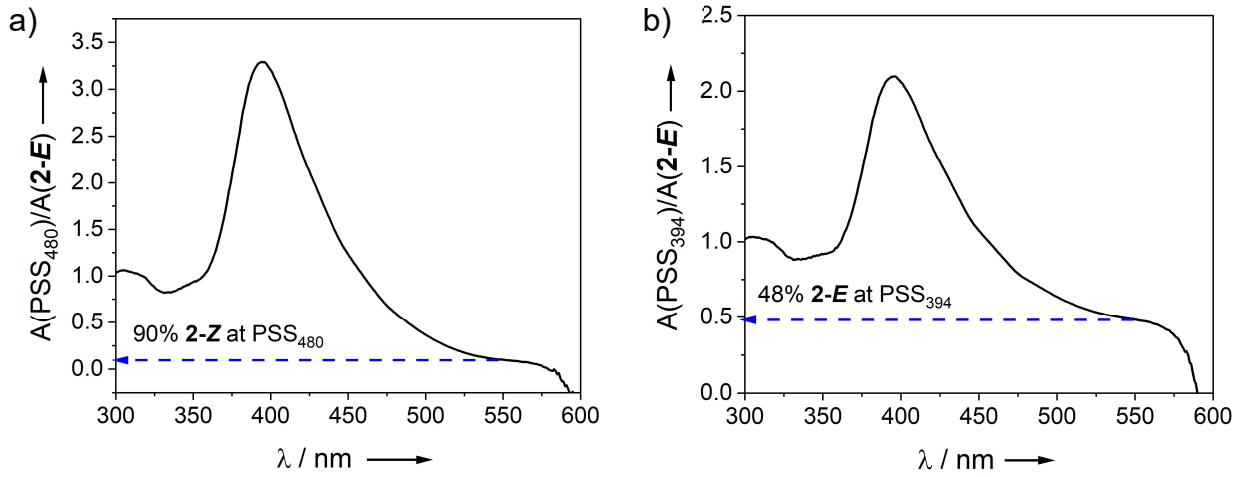

Supplementary Figure S16. Determination of the composition of (a) PSS_{480} and (b) PSS_{394} of hydrazone **2**.

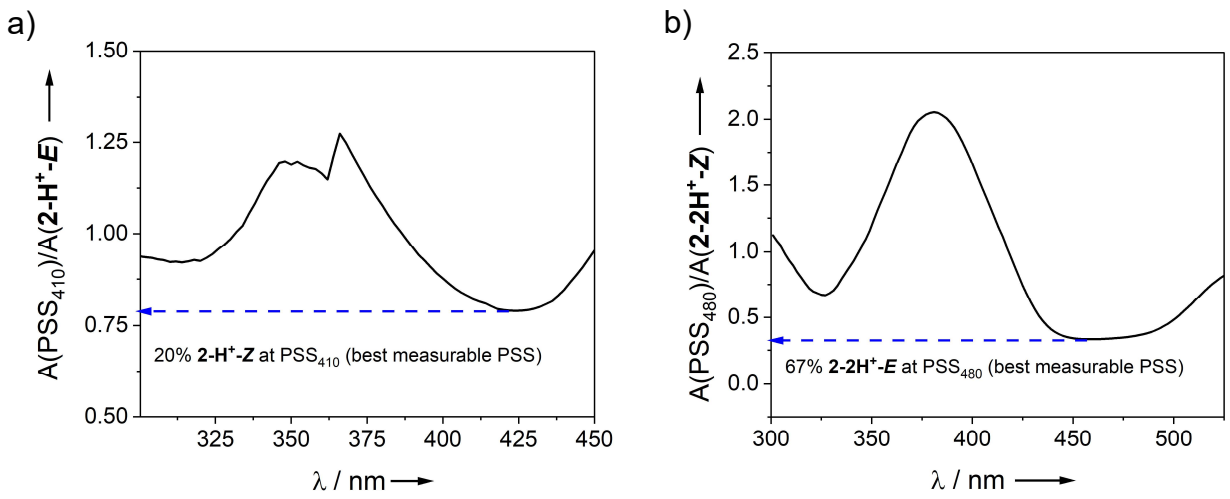

Supplementary Figure S17. Determination of the composition of (a) PSS_{410} of hydrazone **2-H**$^+$ and (b) PSS_{480} of hydrazone **2-2H**$^+$.

5 Photoisomerization Quantum Yields

The quantum yield (Φ) of all the derivatives was determined by following a previously reported procedure.[S7] To describe the kinetic behavior of the isomerization process, we used a first-order kinetic model. The rate of conversion of the *E* isomer to the *Z* isomer is governed by equation 1. Actinometry was performed to determine the flux of light from the irradiation system.[S8] A solution of each of the derivatives in spectroscopic grade toluene was irradiated with the appropriate wavelength of light. The absorbance intensity at a specific wavelength was measured as a function of time. These values were then used to calculate the integrated photokinetic factor $x(t)$ (equation 2). The resulting values of $x(t)$ were plotted against the fraction of the *Z* isomer (y), which was determined using UV-Vis spectroscopy, and the PSS isomer ratios (Supplementary Figures S14–S17). This plot was fitted using equation 4 to determine *R* (equation 3), which is the kinetic rate factor.

$$ln\frac{y_\infty - y}{y_\infty - y_0} = -\frac{I \cdot l \cdot \Phi_{E\to Z} \cdot \varepsilon_E}{V \cdot y_\infty}\int_{t_0}^{t}\frac{1-10^{-A(t)}}{A(t)}dt \qquad \text{Eq. 1}$$

$$x(t) = \int_{t_0}^{t}\frac{1-10^{-A(t)}}{A(t)}dt \qquad \text{Eq. 2}$$

$$R = -\frac{I \cdot l \cdot \Phi_{E\to Z} \cdot \varepsilon_E}{V \cdot y_\infty} \qquad \text{Eq. 3}$$

where $A(t)$ is defined as absorption at time *t*, *V* indicates the volume of solution, y_∞ is the *Z* isomer fraction at the PSS and y_0 is the *Z* isomer fraction at $t = 0$ s, *I* indicates the molar flux of light, ε_E indicates the molar absorptivity and *l* indicates the path length.

The resulting function was fitted using

$$y = y_\infty + Ae^{Rt} \qquad \text{Eq. 4}$$

From this, the quantum yield $\Phi_{E\to Z}$ was determined using:

$$\Phi_{E\to Z} = \frac{R \cdot V \cdot y_\infty}{I_0 \cdot \varepsilon_E \cdot l} \qquad \text{Eq. 5}$$

Typical fits are shown in Supplementary Figures S18–S22. The resulting value for *R* was used in equation 5 to determine $\Phi_{E\to Z}$. The process was repeated to measure $\Phi_{Z\to E}$.

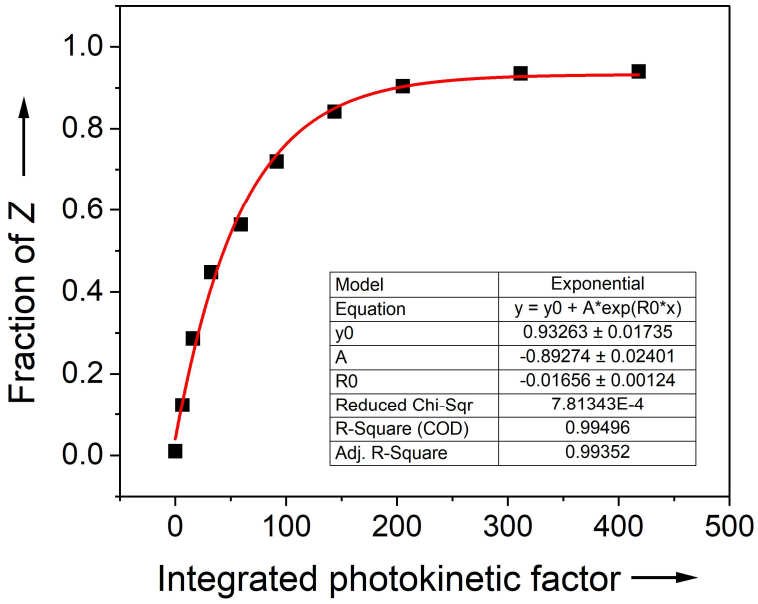

Supplementary Figure S18. Exponential fitting of the *Z* isomer fraction of **1** against the integrated photokinetic factor $x(t)$ upon 515 nm irradiation. $\varepsilon_{\mathbf{1}\text{-}\boldsymbol{E}@515\ \mathrm{nm}}$ = 14,400 $M^{-1}{\cdot}cm^{-1}$ was used for quantum yield calculations. The photoisomerization quantum yield of **1-*E*** to **1-*Z*** in toluene (2.0×10^{-5} M) at 298 K was calculated to be 1.08 ± 0.03 % based on three consecutive measurements.

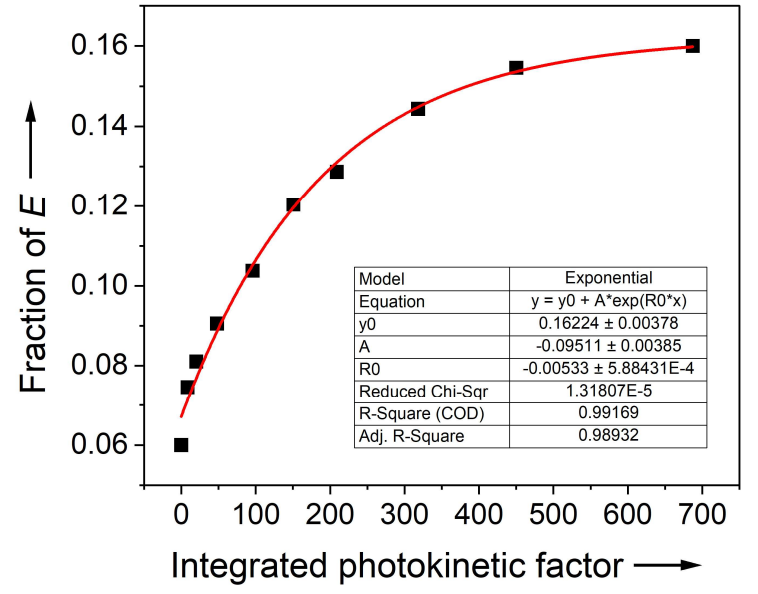

Supplementary Figure S19. Exponential fitting of the *E* isomer fraction of **1** against the integrated photokinetic factor $x(t)$ upon 410 nm irradiation. $\varepsilon_{\mathbf{1}\text{-}\boldsymbol{Z}@410\ \mathrm{nm}}$ = 27,100 $M^{-1}{\cdot}cm^{-1}$ was used for quantum yield calculations. The photoisomerization quantum yield of **1-*Z*** to **1-*E*** in toluene (2.0×10^{-5} M) at 298 K was calculated to be 0.89 ± 0.25 % based on three consecutive measurements.

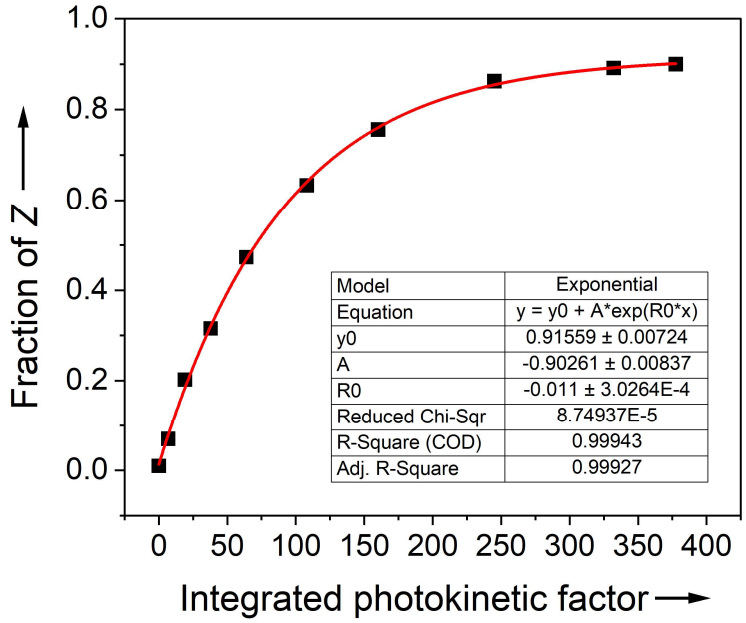

Supplementary Figure S20. Exponential fitting of the *Z* isomer fraction of **2** against the integrated photokinetic factor $x(t)$ upon 480 nm irradiation. $\varepsilon_{\mathbf{2}\text{-}\boldsymbol{E}@480\ nm}$ = 22,900 $M^{-1}{\cdot}cm^{-1}$ was used for quantum yield calculations. The photoisomerization quantum yield of **2-*E*** to **2-*Z*** in toluene (2.0×10^{-5} M) at 298 K was calculated to be 0.56 ± 0.10 % based on three consecutive measurements.

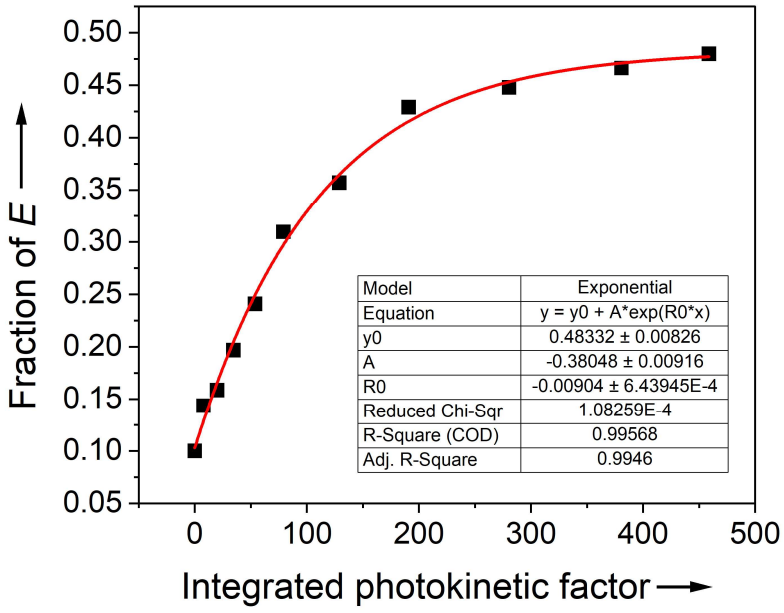

Supplementary Figure S21. Exponential fitting of the *E* isomer fraction of **2** against the integrated photokinetic factor $x(t)$ upon 394 nm irradiation. $\varepsilon_{\mathbf{2}\text{-}\boldsymbol{Z}@394\ nm}$ = 15,400 $M^{-1}{\cdot}cm^{-1}$ was used for quantum yield calculations. The photoisomerization quantum yield of **2-*Z*** to **2-*E*** in toluene (2.0×10^{-5} M) at 298 K was calculated to be 0.11 ± 0.02 % based on three consecutive measurements.

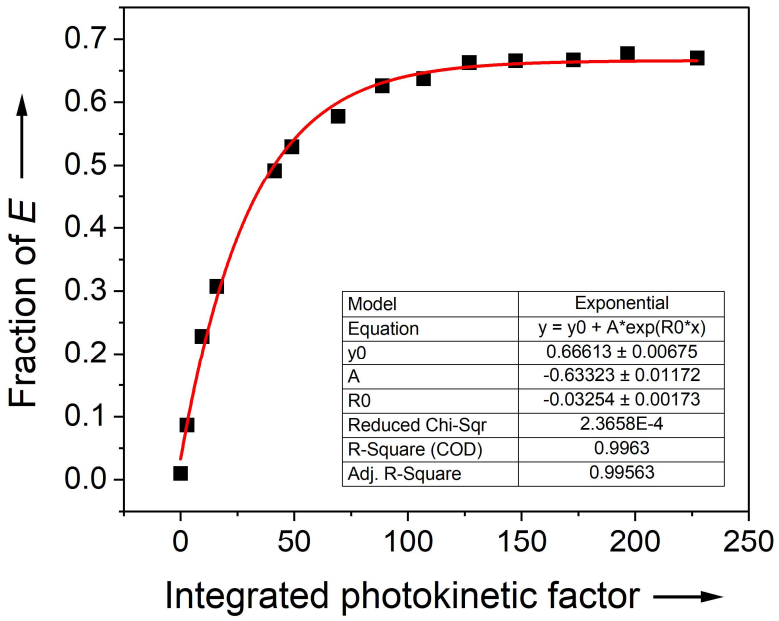

Supplementary Figure S22. Exponential fitting of the *E* isomer fraction of **2** against the integrated photokinetic factor $x(t)$ upon 480 nm irradiation. ε(**2-2H$^+$-*Z*** @480 nm) = 15,200 $M^{-1}\cdot cm^{-1}$ was used for quantum yield calculations. The photoisomerization quantum yield of **2-2H$^+$-*Z*** to **2-2H$^+$-*E*** in toluene (1.95×10^{-5} M) at 298 K was calculated to be 1.31 ± 0.03 % based on three consecutive measurements.

6 Kinetic Studies

The thermal isomerization kinetics of the hydrazones were studied using UV-Vis spectroscopy.[S6] A solution of each of the derivatives in spectroscopic grade toluene was irradiated with the appropriate wavelength to obtain either an *E*-rich (for hydrazones **1-H**$^+$ and **2-2H**$^+$) or a *Z*-rich (for hydrazones **1**, **2**, and **2-H**$^+$) solution.

The change in concentration of the *E* isomer (for **1-H**$^+$ and **2-2H**$^+$) or the *Z* isomer (for **1**, **2**, and **2-H**$^+$) was monitored as a function of time using UV-Vis spectroscopy at room temperature (298 K). The thermal isomerization rate (k_1) was determined by least-square curve fitting using an integrated and combined rate equation (Eq. 8) of a single-species reversible reaction.

$$\mathrm{A} \underset{k_{-1}}{\overset{k_1}{\rightleftharpoons}} \mathrm{B}$$

$$K_{eq} = \frac{\mathrm{k_1}}{k_{-1}} = \frac{C_A^0 - C_A^{eq}}{C_A^{eq}} \qquad \text{Eq. 6}$$

$$\ln \frac{C_A - C_A^{eq}}{C_A^0 - C_A^{eq}} = -(\mathrm{k_1} + \mathrm{k_{-1}})t \qquad \text{Eq. 7}$$

Combining Eq. 6 and 7 will give Eq. 8 as follows,

$$C_A = \left(C_A^0 - C_A^{eq}\right) \times e^{\left(\frac{-k_1 \cdot C_A^0 \cdot t}{C_A^0 - C_A^{eq}}\right)} + C_A^{eq} \qquad \text{Eq. 8}$$

where C_A, C_A^0 , and C_A^{eq} stand for experimental, initial, and equilibrium concentrations of the metastable configuration of the hydrazone switch, respectively; *t* stands for the thermal relaxation time. The reported values were calculated based on three consecutive measurements. Typical fits are shown in Figures S23–S27.

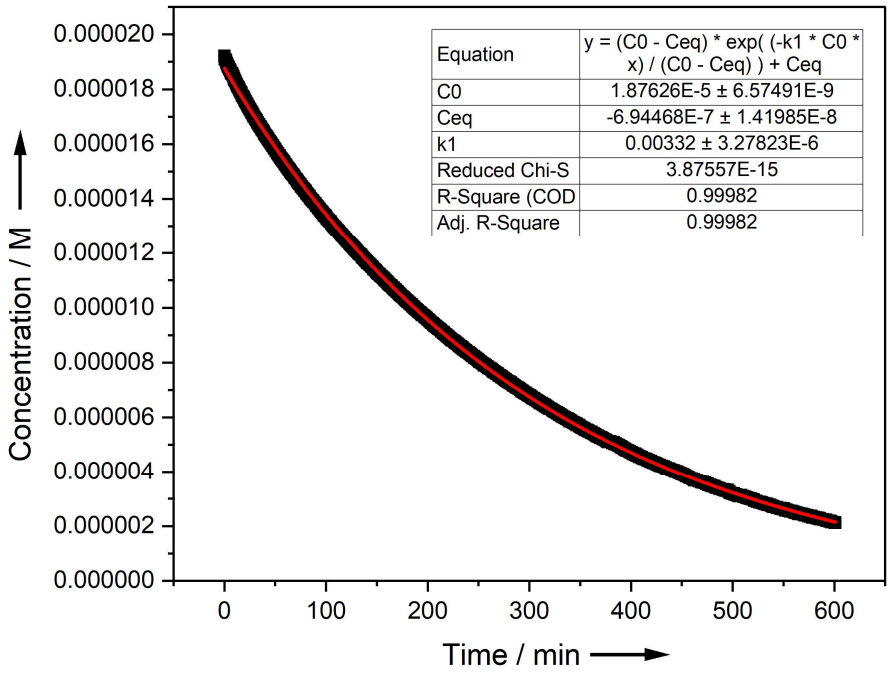

Supplementary Figure S23. Thermal isomerization of **1-*Z*** → **1-*E*** in toluene (2.0×10^{-5} M) at 298 K. The plot is of the concentration of **1-*Z*** as a function of time.

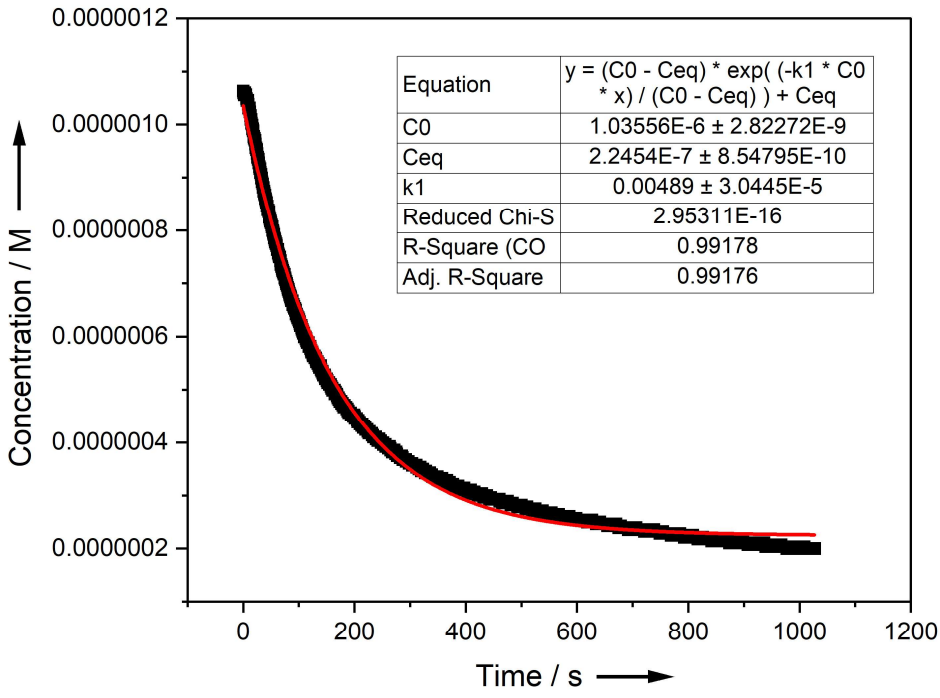

Supplementary Figure S24. Thermal isomerization of **1-H$^+$-*E*** → **1-H$^+$-*Z*** in toluene (1.43×10^{-5} M) at 298 K. The plot is of the concentration of **1-H$^+$-*E*** as a function of time.

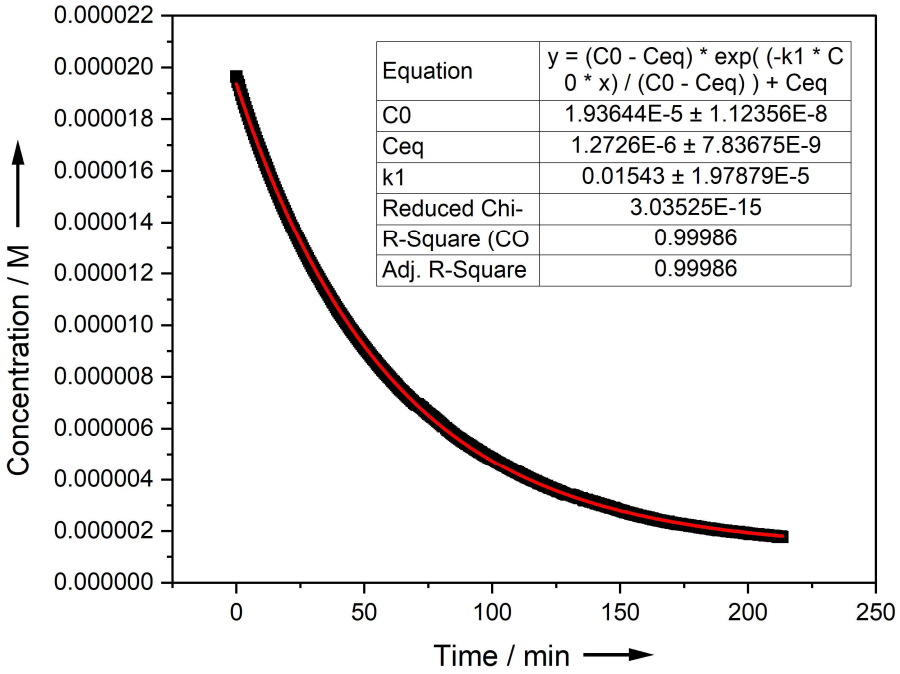

Supplementary Figure S25. Thermal isomerization of **2-*Z*** → **2-*E*** in toluene (2.0×10^{-5} M) at 298 K. The plot is of the concentration of **2-*Z*** as a function of time.

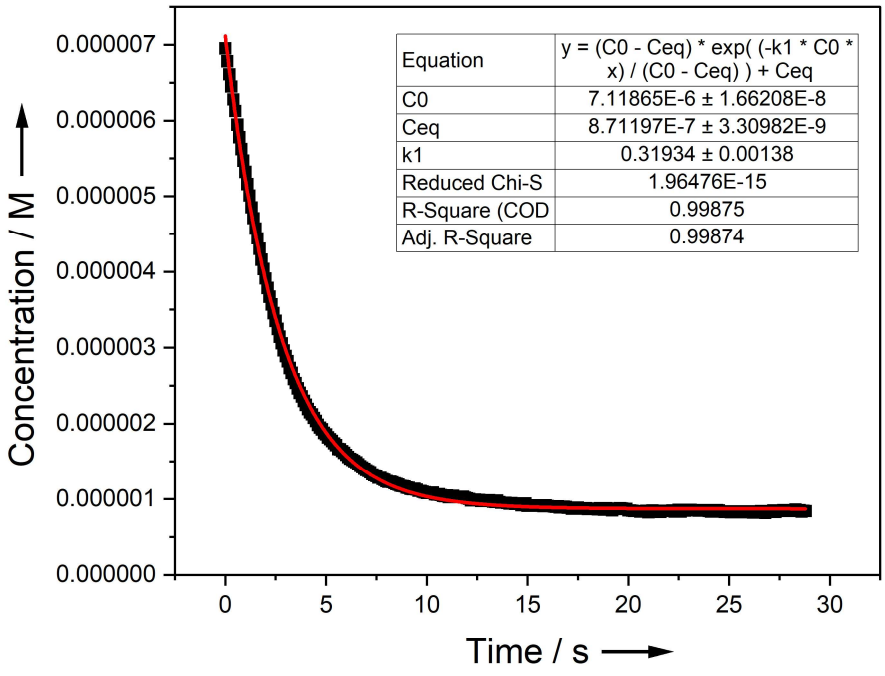

Supplementary Figure S26. Thermal isomerization of **2-H$^+$-*Z*** → **2-H$^+$-*E*** in toluene (1.99×10^{-5} M) at 298 K. The plot is of the concentration of **2-H$^+$-*Z*** as a function of time.

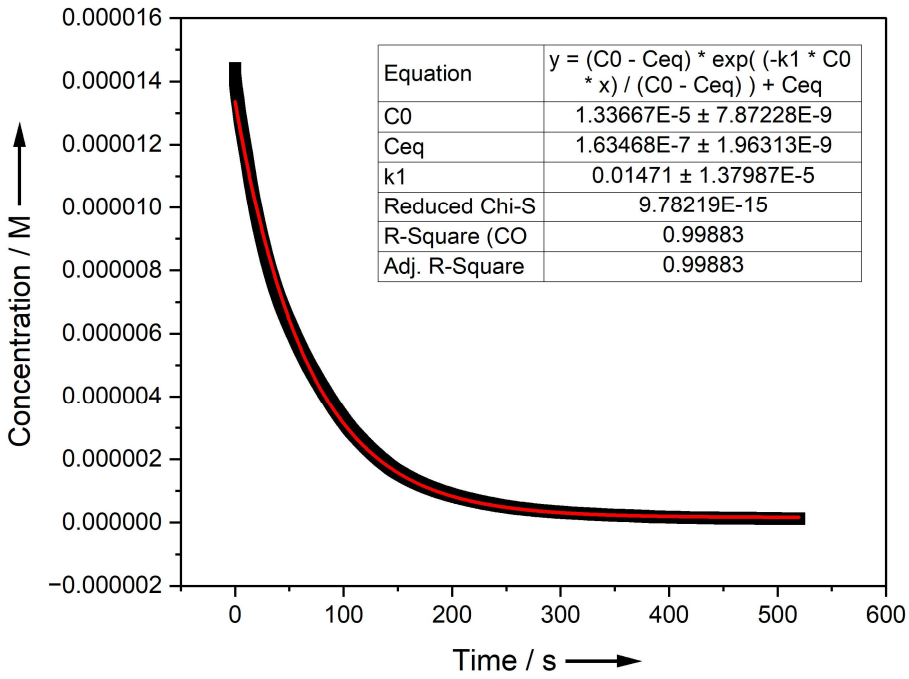

Supplementary Figure S27. Thermal isomerization of **2-2H$^+$-*E*** → **2-2H$^+$-*Z*** in toluene (1.95×10^{-5} M) at 298 K. The plot is of the concentration of **2-2H$^+$-*E*** as a function of time.

Supplementary Table S1. The isomerization rates, energy barriers and half-lives of the hydrazones at 298 K.

Hydrazone	$k_{298\ K}$ (s^{-1})[a]	$\Delta G^{\neq}$ (kcal mol^{-1})[a]	$\tau_{1/2}$
1	$(6.3 \pm 1.7) \times 10^{-5}$	23.2 ± 0.2	3.3 ± 0.8 h
1-H$^+$	$(4.6 \pm 0.3) \times 10^{-3}$	20.6 ± 0.1	2.5 ± 0.2 min
2	$(2.9 \pm 0.2) \times 10^{-4}$	22.3 ± 0.1	39.9 ± 3.6 min
2-H$^+$	$(2.7 \pm 0.4) \times 10^{-1}$	18.2 ± 0.1	2.6 ± 0.3 s
2-2H$^+$	$(1.5 \pm 0.1) \times 10^{-2}$	19.9 ± 0.1	46.6 ± 0.5 s

[a]Average of three measurements.

7 Computational Methods and Results

DFT optimizations for all plausible conformers were carried out using the M06-2X functional and the 6-311++G(d,p) basis set for all atoms as implemented in Gaussian 16.[S9] The SMD solvation model was employed to simulate a non-polar environment, specifically in toluene.[S10] Frequency analysis was performed to confirm the nature of the identified states. This analysis ensured that the minimum energy structures had no imaginary frequencies. Thermodynamic correction properties were derived from these frequency calculations. The energy-minimized ground state structures are shown in Supplementary Figures S28–S32. Time-dependent density functional theory (TD-DFT) calculations were performed to simulate the UV-Vis absorption spectra of all compounds in both *E* and *Z* configurations. The six lowest energy singlet excited states were predicted. The linear solvation model was applied throughout the calculations to account for solvent effects. Supplementary Figures S33 and S34 show the calculated HOMOs and LUMOs along with the HOMO–LUMO energy gaps. In all the compounds the HOMO–LUMO transition is the dominant contributor to the bright state ($S_0 \rightarrow S_1$). However, the optical gaps or vertical excitation energies (VEEs) are more precise indicators of spectral properties in comparison to the purely electronic (HOMO–LUMO) gaps. Supplementary Tables S2–S6 summarize the VEEs and the involved MOs for the two lowest singlet excited state transitions for all compounds, and Supplementary Figures S40 and S41 show the corresponding spectra reflecting the energy gaps. Supplementary Figures S35–S39 show natural transition orbital (NTO) representations for these transitions.[S11]

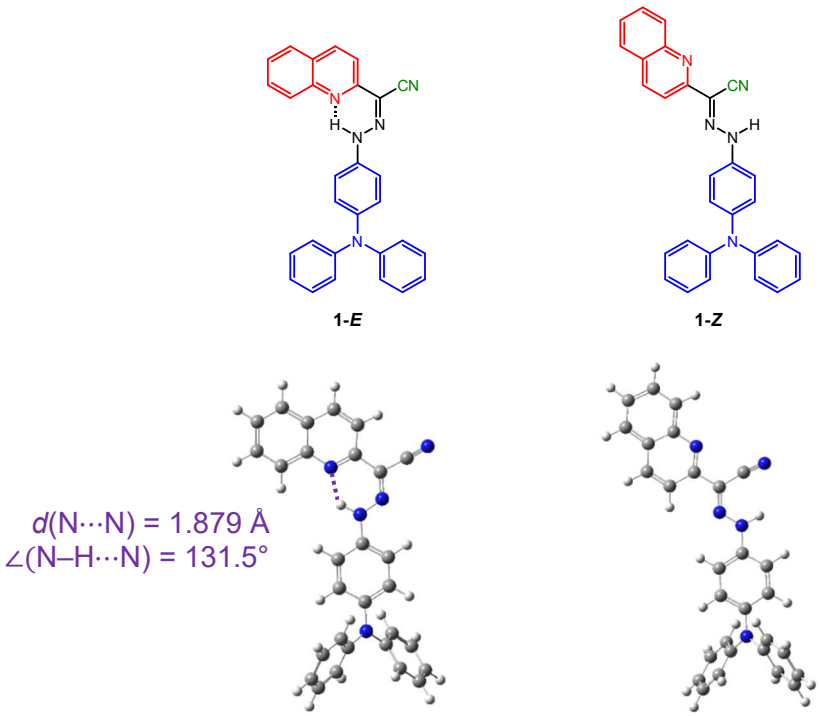

Supplementary Figure S28. Chemical structures and the ground-state optimized geometries of **1-*E*** and **1-*Z***. *E* is 2.0 kcal mol^{-1} lower in energy than *Z*. Insets highlight the H-bond parameters.

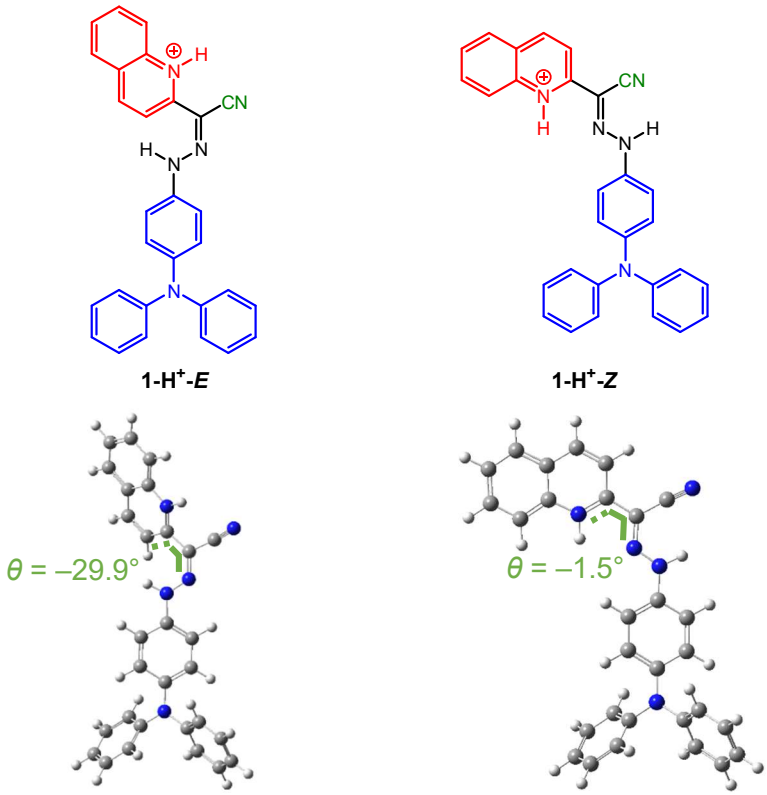

Supplementary Figure S29. Chemical structures and the ground-state optimized geometries of **1-H$^+$-*E*** and **1-H$^+$-*Z***. *Z* is 11.7 kcal mol^{-1} lower in energy than *E*. Insets highlight key dihedral angles.

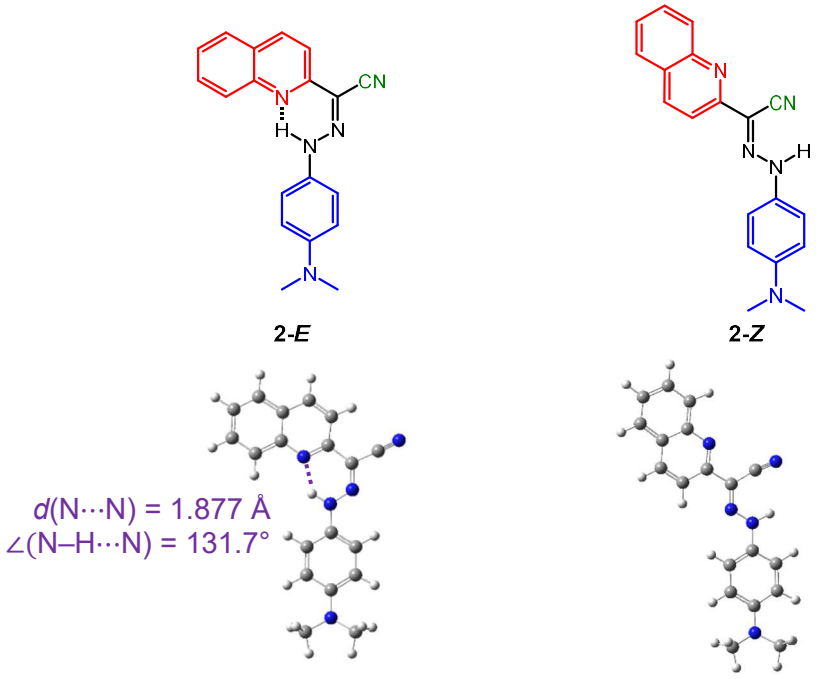

Supplementary Figure S30. Chemical structures and the ground-state optimized geometries of **2-*E*** and **2-*Z***. *E* is 1.8 kcal mol^{-1} lower in energy than *Z*. Insets highlight the H-bond parameters.

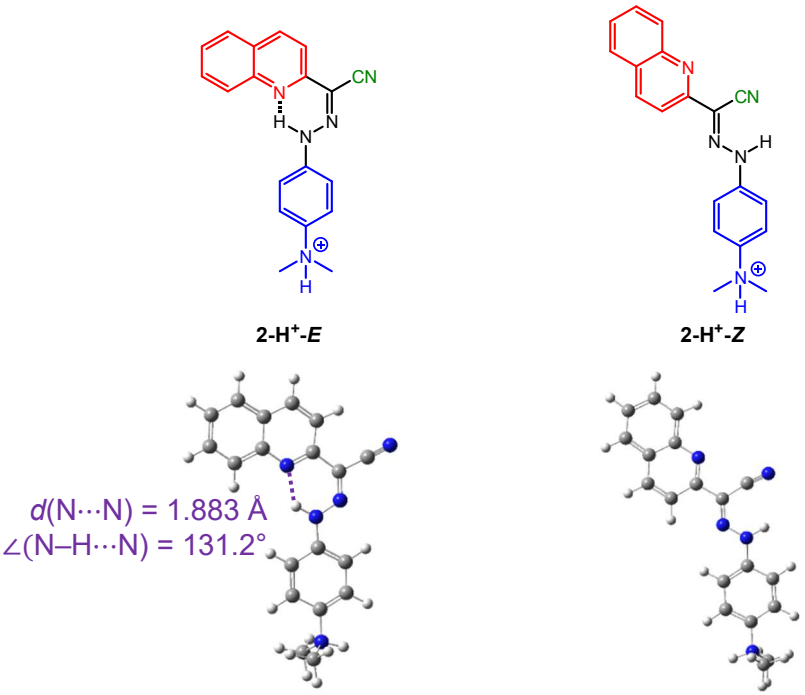

Supplementary Figure S31. Chemical structures and the ground-state optimized geometries of **2-H$^+$-*E*** and **2-H$^+$-*Z***. *E* is 3.0 kcal mol^{-1} lower in energy than *Z*. Insets highlight the H-bond parameters.

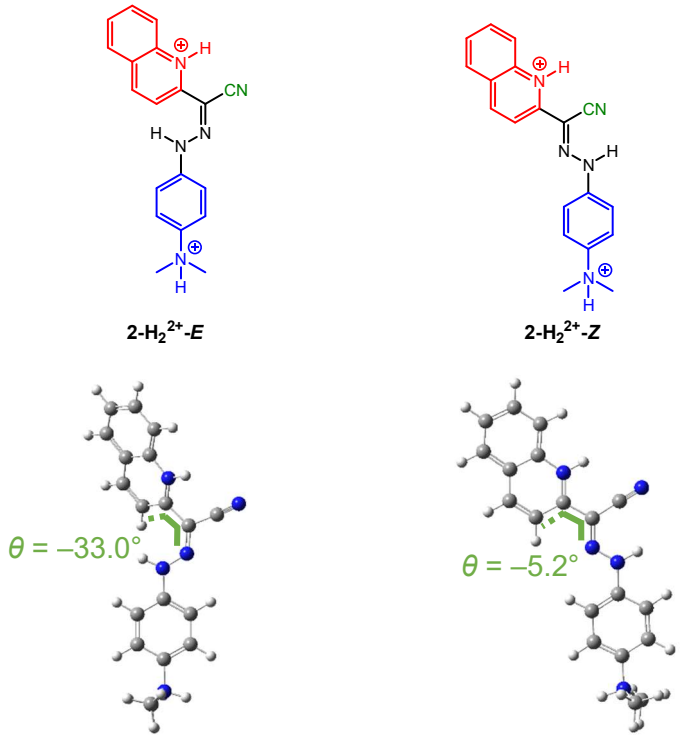

Supplementary Figure S32. Chemical structures and the ground-state optimized geometries of **2-2H$^+$-*E*** and **2-2H$^+$-*Z***. *Z* is 8.8 kcal mol^{-1} lower in energy than *E*. Insets highlight key dihedral angles.

Supplementary Table S2. Vertical excitation energies (VEEs), oscillator strengths (*f*), and the involved MOs for the two lowest singlet excited state transitions of both isomers of **1**.

1-*E*				**1-*Z***			
Transition	VEE (eV) (nm)	*f*	MOs (|weight|)	Transition	VEE (eV) (nm)	*f*	MOs (|weight|)
$S_0 \rightarrow S_1$	3.00 (413)	0.966	114 → 116 (0.25) 115 → 116 (0.63) 115 → 117 (0.12)	$S_0 \rightarrow S_1$	3.17 (392)	1.234	114 → 116 (0.23) 115 → 116 (0.64) 115 → 117 (0.10)
$S_0 \rightarrow S_2$	3.94 (314)	0.020	114 → 116 (0.13) 115 → 117 (0.15) 115 → 118 (0.49) 115 → 119 (0.35) 115 → 120 (0.23)	$S_0 \rightarrow S_2$	3.93 (315)	0.109	115 → 117 (0.10) 115 → 118 (0.56) 115 → 119 (0.32) 115 → 120 (0.15)

Supplementary Table S3. Vertical excitation energies (VEEs), oscillator strengths (*f*), and the involved MOs for the two lowest singlet excited state transitions of both isomers of **1-H$^+$**.

1-H$^+$-*E*				**1-H$^+$-*Z***			
Transition	VEE (eV) (nm)	*f*	MOs (|weight|)	Transition	VEE (eV) (nm)	*f*	MOs (|weight|)
$S_0 \rightarrow S_1$	2.08 (596)	0.888	114 → 116 (0.18) 115 → 116 (0.67) 115 → 117 (0.10)	$S_0 \rightarrow S_1$	2.15 (577)	0.982	114 → 116 (0.17) 115 → 116 (0.67) 115 → 117 (0.10)
$S_0 \rightarrow S_2$	3.34 (371)	0.313	114 → 116 (0.20) 114 → 117 (0.18) 115 → 116 (0.18) 115 → 117 (0.59) 115 → 118 (0.11)	$S_0 \rightarrow S_2$	3.50 (354)	0.254	108 → 116 (0.17) 113 → 116 (0.19) 114 → 116 (0.61) 115 → 116 (0.19)

Supplementary Table S4. Vertical excitation energies (VEEs), oscillator strengths (*f*), and the involved MOs for the two lowest singlet excited state transitions of both isomers of **2**.

2-*E*				**2-*Z***			
Transition	VEE (eV) (nm)	*f*	MOs (|weight|)	Transition	VEE (eV) (nm)	*f*	MOs (|weight|)
$S_0 \rightarrow S_1$	2.98 (416)	0.876	82 → 84 (0.14) 83 → 84 (0.67) 83 → 85 (0.11)	$S_0 \rightarrow S_1$	3.17 (392)	1.166	82 → 84 (0.10) 83 → 84 (0.67) 83 → 85 (0.13)
$S_0 \rightarrow S_2$	4.12 (301)	0.092	81 → 84 (0.16) 82 → 84 (0.10) 82 → 85 (0.19) 83 → 85 (0.58) 83 → 89 (0.14) 83 → 91 (0.13) 83 → 92 (0.14)	$S_0 \rightarrow S_2$	4.10 (302)	0.101	81 → 84 (0.18) 82 → 85 (0.25) 83 → 85 (0.58) 83 → 90 (0.15)

Supplementary Table S5. Vertical excitation energies (VEEs), oscillator strengths (*f*), and the involved MOs for the two lowest singlet excited state transitions of both isomers of **2-H$^+$**.

2-H$^+$-*E*				**2-H$^+$-*Z***			
Transition	VEE (eV) (nm)	*f*	MOs (|weight|)	Transition	VEE (eV) (nm)	*f*	MOs (|weight|)
$S_0 \rightarrow S_1$	3.56 (348)	0.900	83 → 84 (0.69)	$S_0 \rightarrow S_1$	3.69 (336)	1.324	82 → 84 (0.18) 83 → 84 (0.67)
$S_0 \rightarrow S_2$	4.20 (295)	0.000	80 → 84 (0.66)	$S_0 \rightarrow S_2$	4.24 (292)	0.015	81 → 86 (0.10) 81 → 87 (0.12) 82 → 84 (0.58) 82 → 86 (0.13) 82 → 89 (0.11) 82 → 95 (0.11) 83 → 84 (0.14) 83 → 86 (0.13) 83 → 87 (0.16)

Supplementary Table S6. Vertical excitation energies (VEEs), oscillator strengths (*f*), and the involved MOs for the two lowest singlet excited state transitions of both isomers of **2-2H**$^+$.

2-2H$^+$-*E*				**2-2H$^+$-*Z***			
Transition	VEE (eV) (nm)	*f*	MOs (|weight|)	Transition	VEE (eV) (nm)	*f*	MOs (|weight|)
$S_0 \rightarrow S_1$	3.27 (379)	0.944	83 → 84 (0.68) 83 → 85 (0.10)	$S_0 \rightarrow S_1$	3.33 (372)	1.400	83 → 84 (0.68)
$S_0 \rightarrow S_2$	3.82 (325)	0.042	82 → 84 (0.68) 82 → 85 (0.13)	$S_0 \rightarrow S_2$	3.95 (314)	0.049	82 → 84 (0.65) 82 → 85 (0.21)

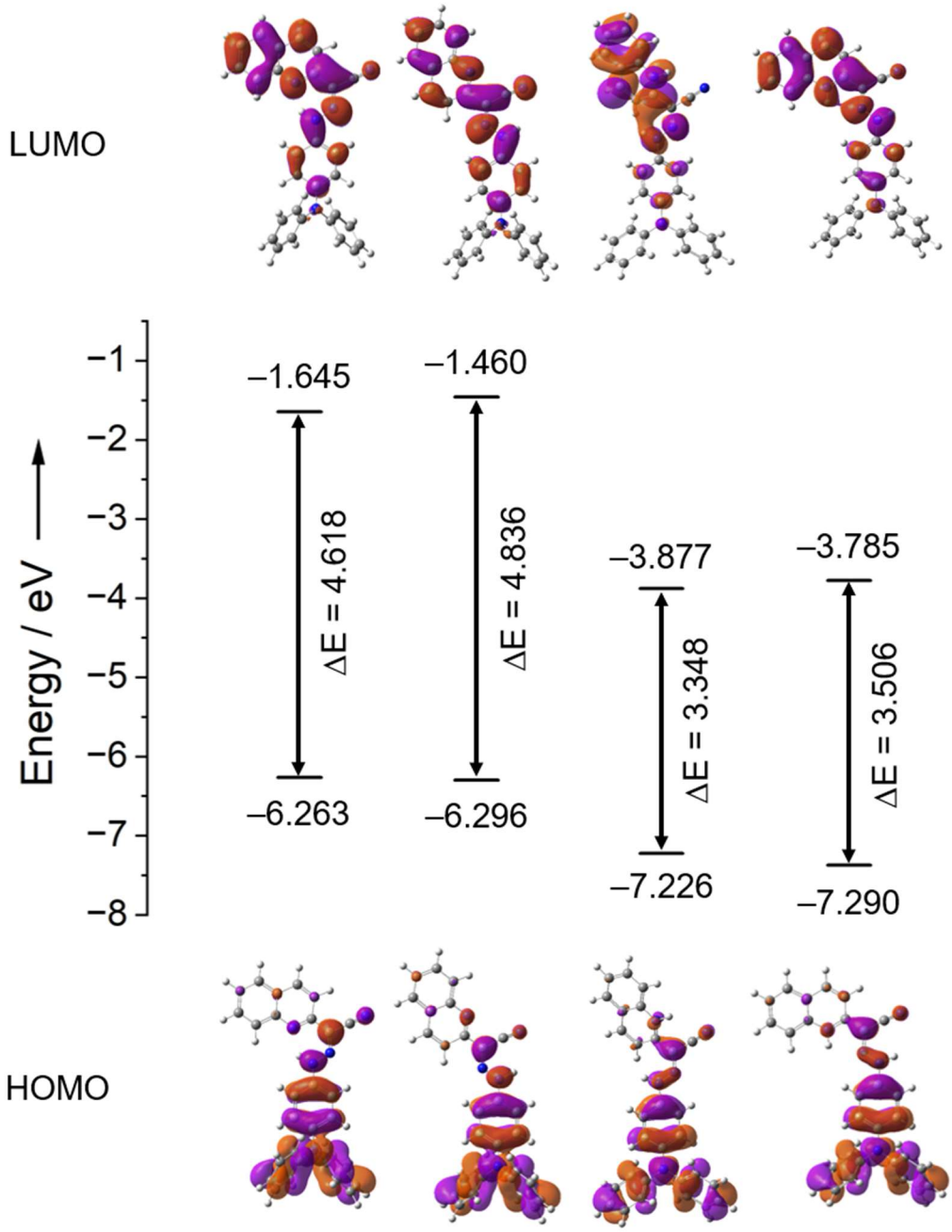

Supplementary Figure S33. Calculated HOMO and LUMO energy levels of compounds **1** and **1-H**$^{+}$ in both their *E* and *Z* configurations.

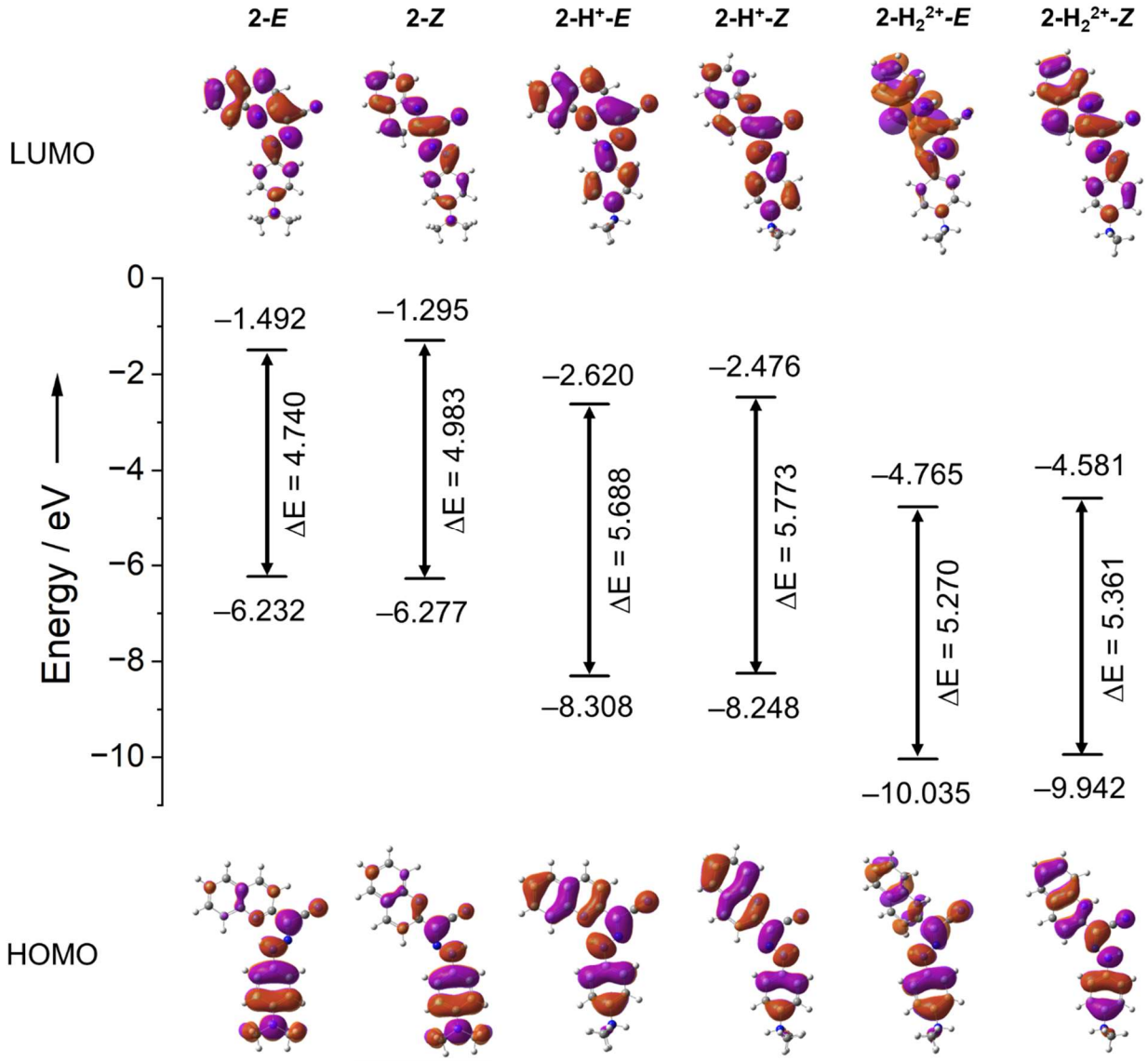

Supplementary Figure S34. Calculated HOMO and LUMO energy levels of compounds **2**, **2-H**$^+$, and **2-2H**$^+$ in both their *E* and *Z* configurations.

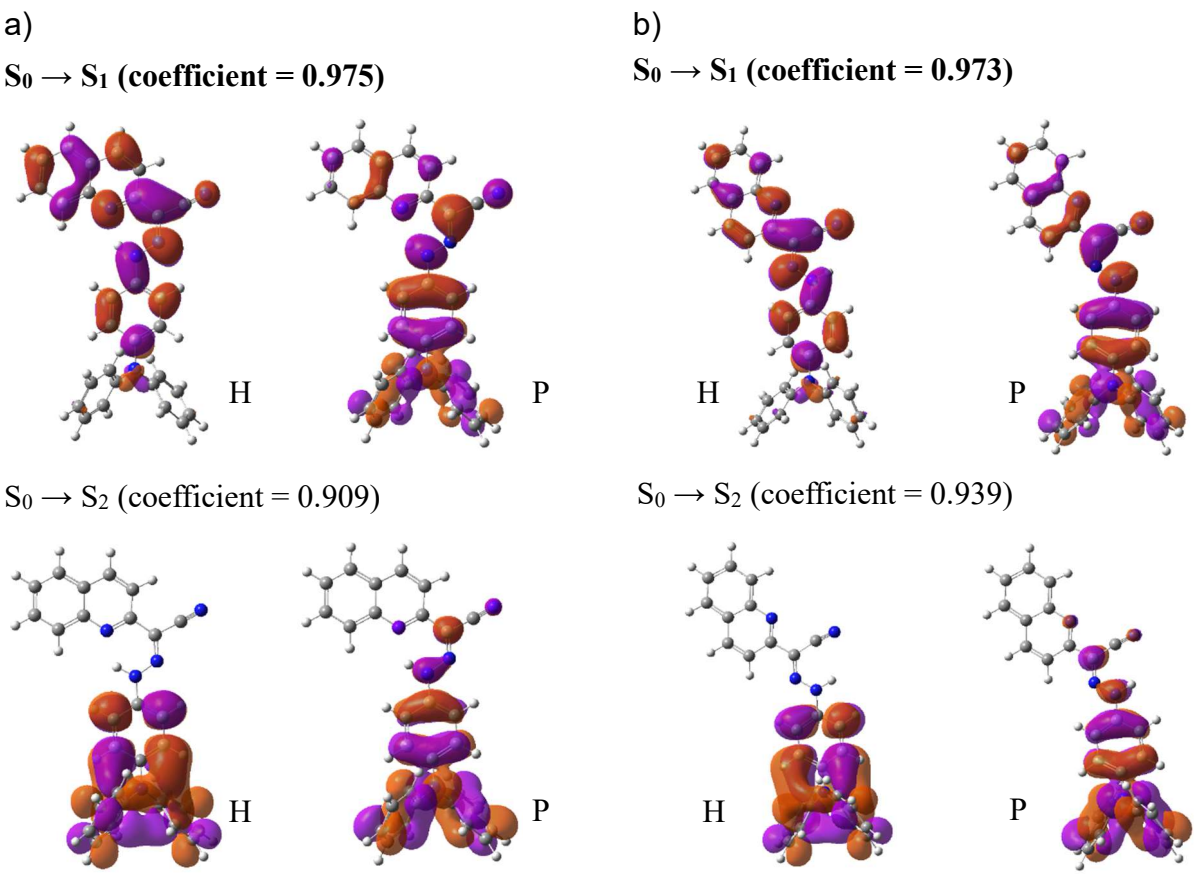

Supplementary Figure S35. Calculated hole (H) and particle (P) natural transition orbitals (NTOs) and their coefficients involved in the two lowest energy transitions for (a) **1-*E*** and (b) **1-*Z***. The transition with the higher oscillator strength is highlighted in bold for both isomers.

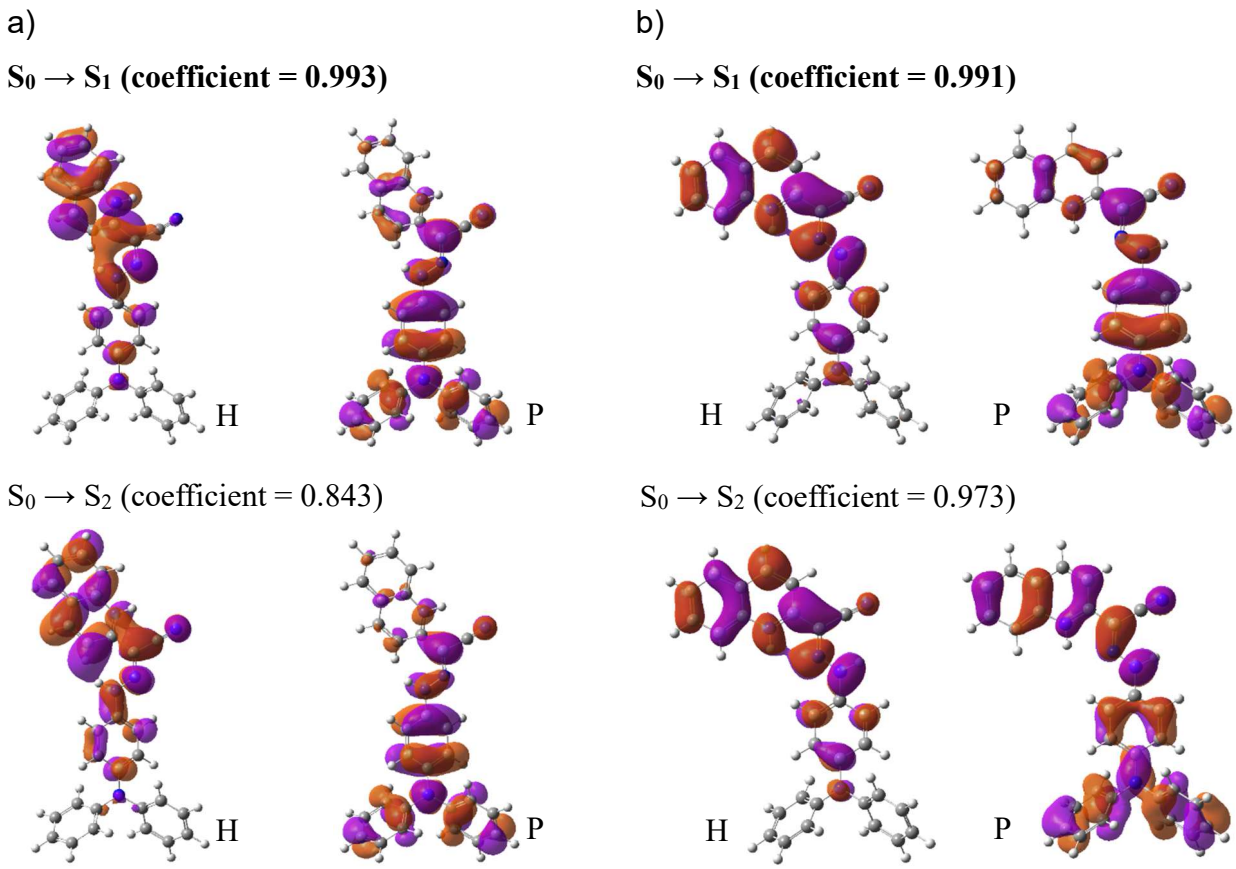

Supplementary Figure S36. Calculated hole (H) and particle (P) natural transition orbitals (NTOs) and their coefficients involved in the two lowest energy transitions for (a) **1-H$^+$-*E*** and (b) **1-H$^+$-*Z***. The transition with the higher oscillator strength is highlighted in bold for both isomers.

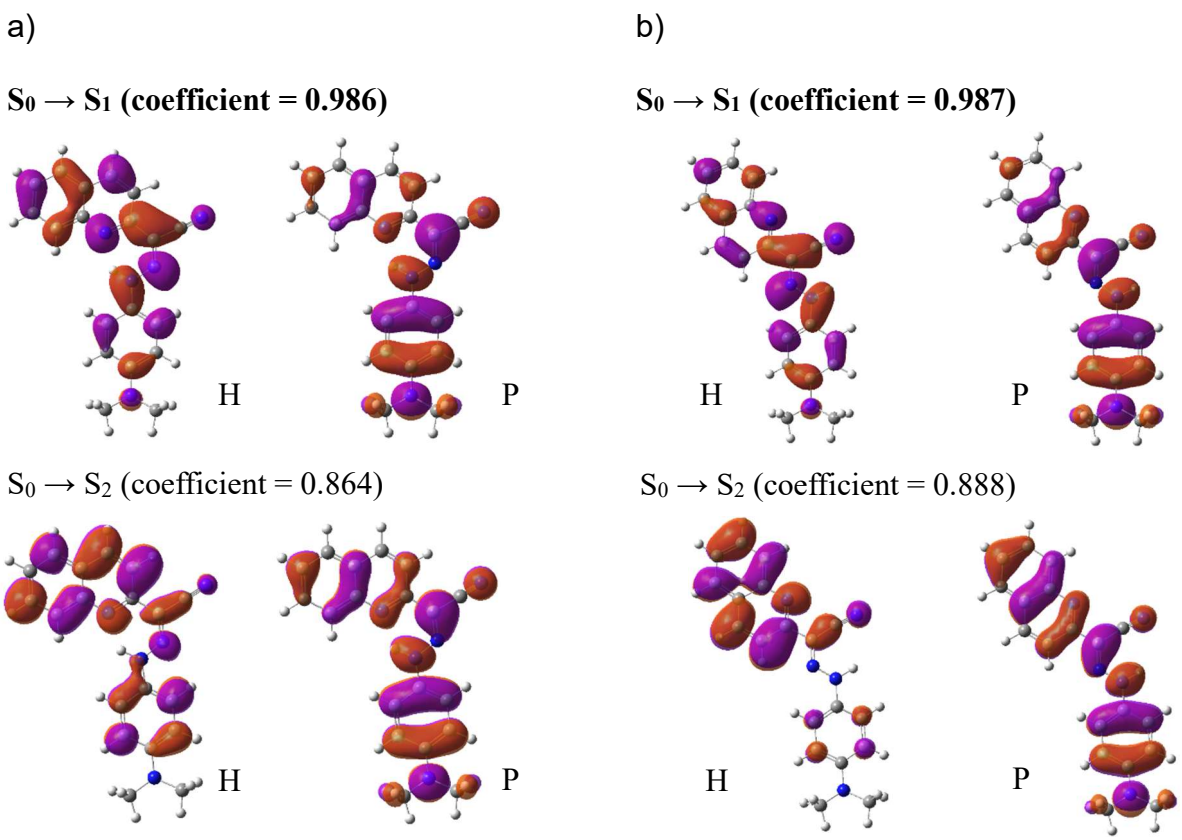

Supplementary Figure S37. Calculated hole (H) and particle (P) natural transition orbitals (NTOs) and their coefficients involved in the two lowest energy transitions for (a) **2-*E*** and (b) **2-*Z***. The transition with the higher oscillator strength is highlighted in bold for both isomers.

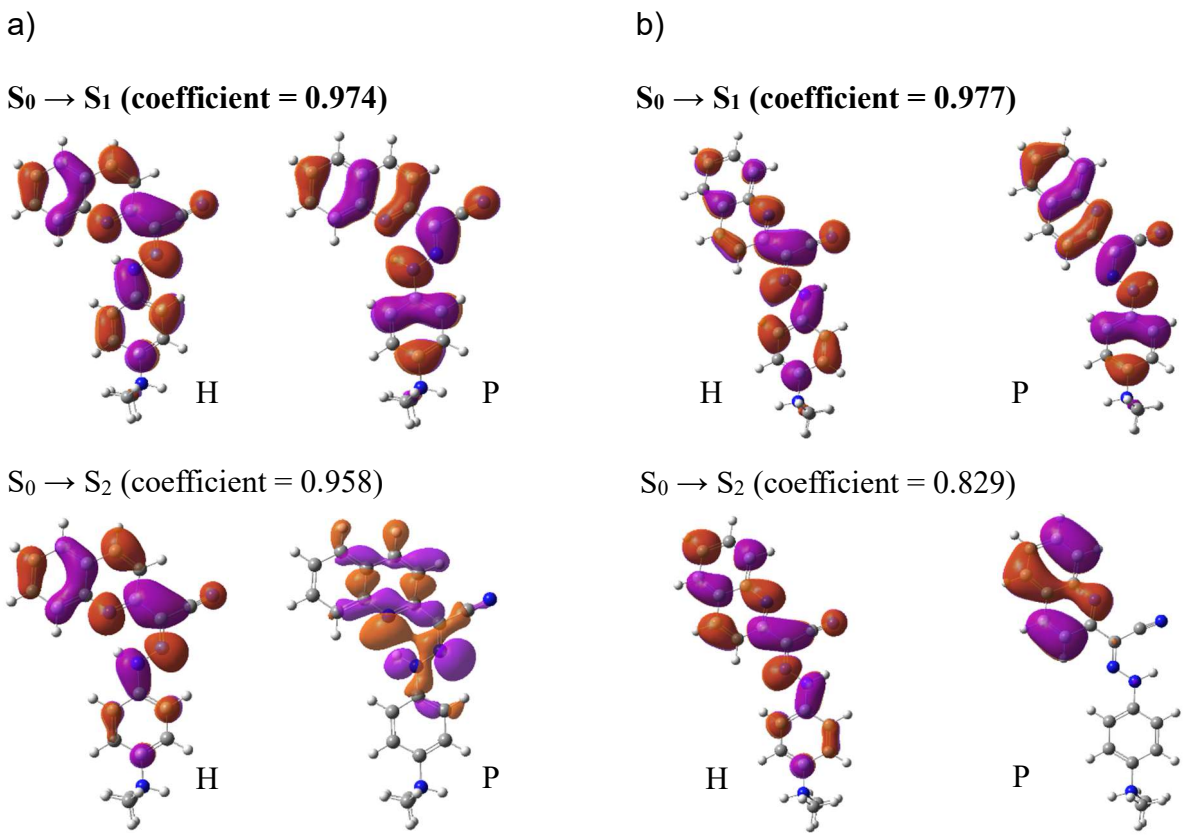

Supplementary Figure S38. Calculated hole (H) and particle (P) natural transition orbitals (NTOs) and their coefficients involved in the two lowest energy transitions for (a) **2-H$^+$-*E*** and (b) **2-H$^+$-*Z***. The transition with the higher oscillator strength is highlighted in bold for both isomers.

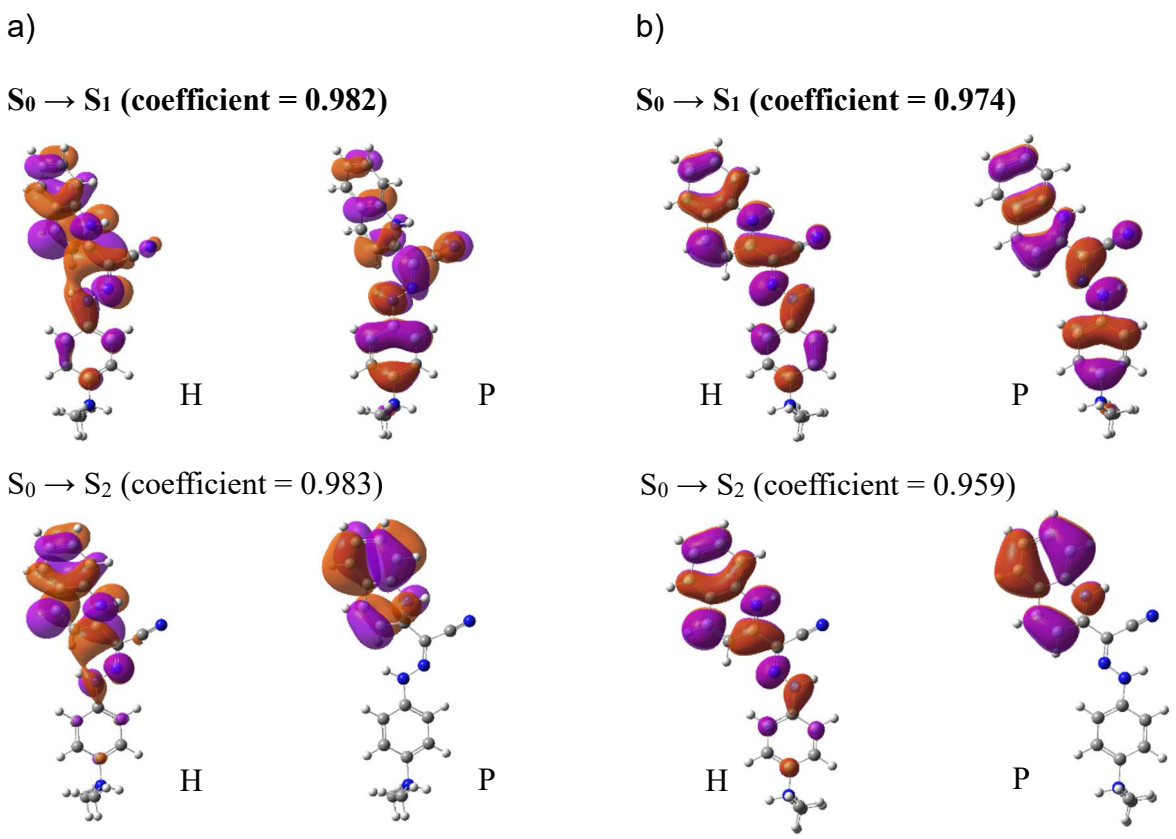

Supplementary Figure S39. Calculated hole (H) and particle (P) natural transition orbitals (NTOs) and their coefficients involved in the two lowest energy transitions for (a) **2-2H$^+$-*E*** and (b) **2-2H$^+$-*Z***. The transition with the higher oscillator strength is highlighted in bold for both isomers.

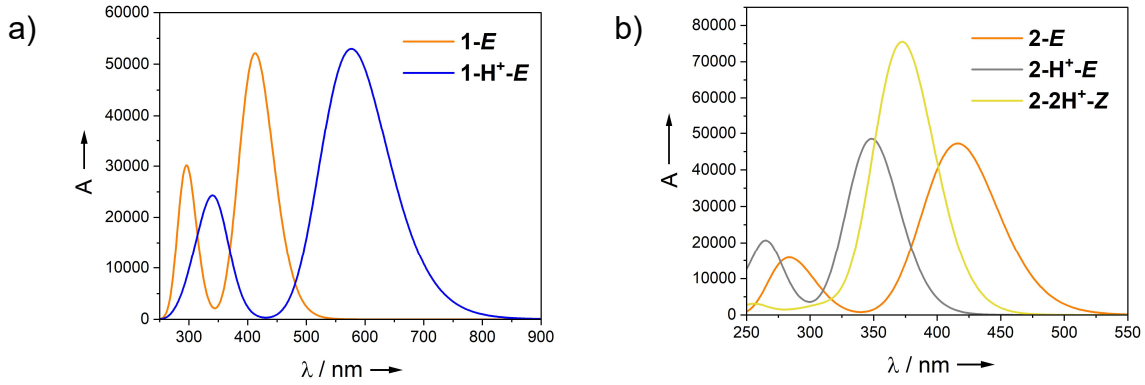

Supplementary Figure S40. Simulated UV-Vis absorption spectra of the neutral and protonated forms of (a) **1** and (b) **2**.

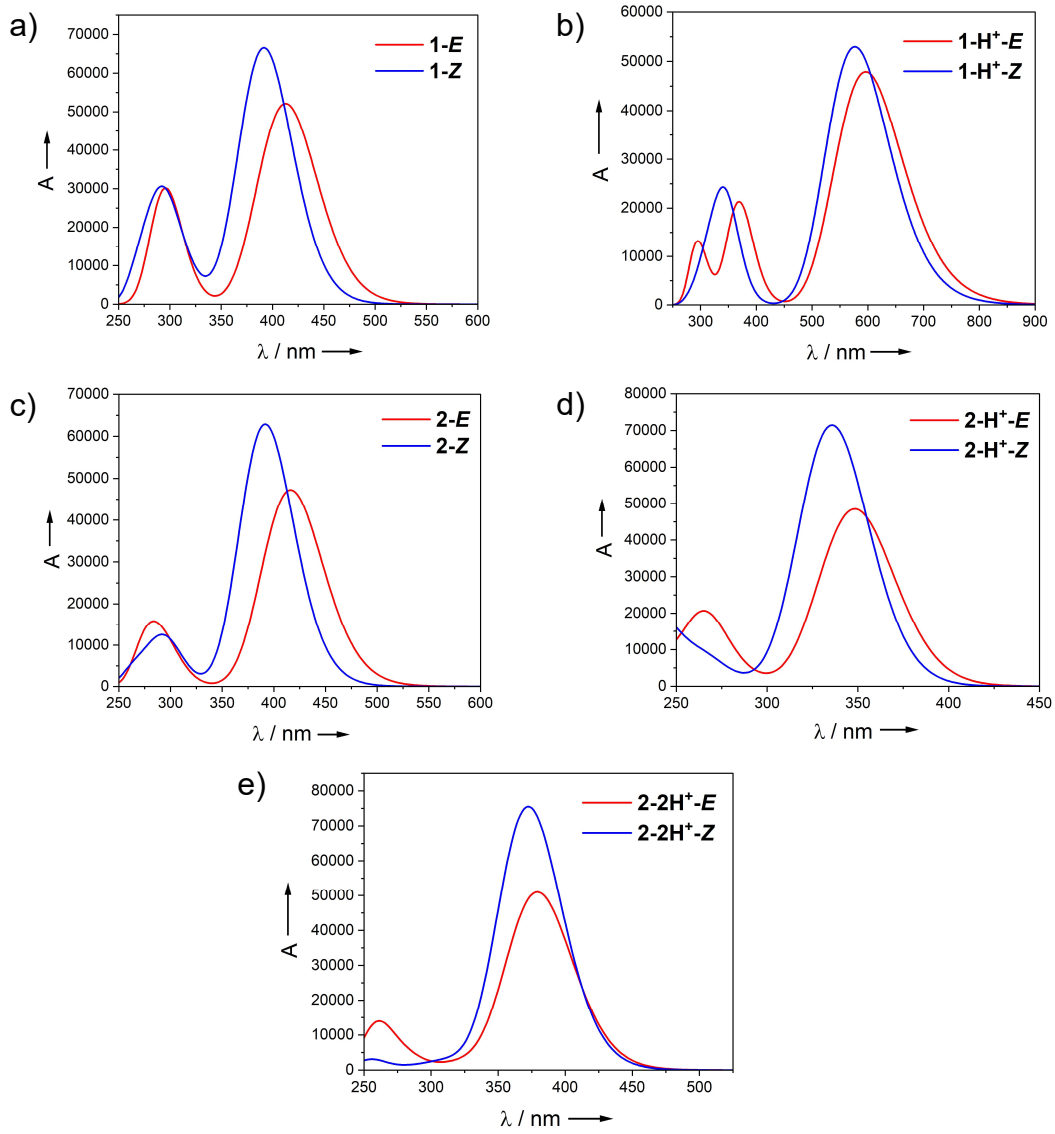

Supplementary Figure S41. Simulated UV-Vis absorption spectra of (a) **1**, (b) **1-H$^+$**, (c) **2**, (d) **2-H$^+$**, and (e) **2-2H$^+$** in both their *E* and *Z* configurations.

8 References

S1. Mangione, M. I., Spanevello, R. A. & Anzardi. M. B. Efficient and straightforward click synthesis of structurally related dendritic triazoles. *RSC. Adv.* **7**, 47681–47688 (2017).
S2. Petrus, M. L. *et al*. Conjugated poly(azomethine)s via simple one-step polycondensation chemistry: Synthesis, thermal and optoelectronic properties. *Polym. Chem.* **4**, 4182–4191 (2013).
S3. Yang, Y., Hughes, R. P. & Aprahamian, I. Near-infrared light activated azo-BF_2 switches. *J. Am. Chem. Soc.* **136**, 13190–13193 (2014).
S4. Hibbert, D. B. & Thordarson, P. The death of the Job plot, transparency, open science and online tools, uncertainty estimation methods and other developments in supramolecular chemistry data analysis. *Chem. Commun.* **52**, 12792–12805 (2016).
S5. Huang, C. Y. *et al*. *N*,*N*′-Disubstituted indigos as readily available red-light photoswitches with tunable thermal half-lives. *J. Am. Chem. Soc*. **139**, 15205−15211 (2017).
S6. Shao, B., Qian, H., Li, Q. & Aprahamian, I. Structure property analysis of the solution and solid-state properties of bistable photochromic hydrazones. *J. Am. Chem. Soc*. **141**, 8364−8371 (2019).
S7. He, Y. *et al*. Azobispyrazole family as photoswitches combining (near-) quantitative bidirectional isomerization and widely tunable thermal half-lives from hours to years. *Angew. Chem., Int. Ed.* **60**, 16539–16546 (2021).
S8. Kuhn, H. J., Braslavsky, S. E. & Schmidt, R. Chemical actinometry (IUPAC technical report). *Pure Appl. Chem.* **76**, 2105–2146 (2004).
S9. Frisch, M. J. *et al*. Gaussian 16, Rev. C.01, Gaussian, Inc., (Wallingford CT, USA) (2016).
S10. Tomasi, J., Mennucci, B. & Cammi, R. Quantum mechanical continuum solvation models. *Chem. Rev.* **105**, 2999–3094 (2005).
S11. Martin, R. L. Natural transition orbitals. *J. Chem. Phys.* **118**, 4775–4777 (2003).